

Taylor bubble motion in stagnant and flowing liquids in vertical pipes. Part II: Linear stability analysis

H. A. Abubakar^{1,2} and O. K. Matar^{1†}

¹Department of Chemical Engineering, Imperial College London, London SW7 2AZ, UK

²Department of Chemical Engineering, Ahmadu Bello University, Zaria 810107, Nigeria

(Received xx; revised xx; accepted xx)

In this study, we examine the linear stability of an axisymmetric Taylor bubble moving steadily in a flowing liquid enclosed in a circular tube. Linearisation is performed about axisymmetric base states obtained in Part I of this study by Abubakar & Matar (2021). The stability is characterised by the dimensionless inverse viscosity (Nf), Eötvös (Eo), and Froude numbers (U_m), the latter being based on the centreline liquid velocity. The analysis shows that there exist regions of (Nf, Eo, U_m) space within which the bubble is unstable and assumes an asymmetric shape. To elucidate the mechanisms underlying the instability, an energy budget analysis is carried out which reveals that perturbation growth is driven by the bubble pressure for $Eo \geq 100$, and by the tangential interfacial stress for $Eo < 100$. Examples of the asymmetric bubble shapes and their associated flow fields are also provided near the onset of instability for a wide range of Nf , Eo , and U_m .

1. Introduction

Slug formation in gas-liquid flows is characterised by intermittent flow of large gas bubbles, separated by liquid masses. In vertical circular tubes, these large bubbles are bullet-shaped with diameter approximately equal to that of the tube, and are known as *Taylor bubbles*. Because of the pseudo-periodic nature of the motion of these bubbles, the study of the behaviour of a single Taylor bubble is considered as a paradigm for understanding the slug flow regime in vertical tubes. For this reason, extensive experimental (Bugg & Saad 2002; Campos & Guedes de Carvalho 1988; Fershtman *et al.* 2017; Griffith & Wallis 1961; Llewellyn *et al.* 2012; Moissis & Griffith 1962; Nicklin *et al.* 1962; Nogueira *et al.* 2006; Pringle *et al.* 2015; Rana *et al.* 2015; White & Beardmore 1962), and a number of theoretical studies (Brown 1965; Collins *et al.* 1978; Dumitrescu 1943; Fabre 2016; Funada *et al.* 2005) have been carried out to examine the steady bubble shape, rise speed, and velocity field surrounding the bubble. In addition, numerical simulations have also been performed a large proportion of which are for axisymmetric bubbles (Bugg & Saad 2002; Kang *et al.* 2010; Lu & Prosperetti 2009; Mao & Dukler 1990, 1991; Taha & Cui 2006), with comparatively fewer studies focusing on the fully three-dimensional case (Anjos *et al.* 2014; Lizarraga-Garcia *et al.* 2017; Taha & Cui 2006).

The shape of the Taylor bubble ‘nose’ plays an important role in determining the rise speed, an important feature for developing predictive models for the slug flow regime (Mao & Dukler 1990). A Taylor bubble rising in a stagnant, or upward-flowing liquid, is generally axisymmetric and moves at constant speed in an inertia-dominated regime. This is not the case for Taylor bubbles moving in downward-flowing liquids, however,

† Email address for correspondence: o.matar@imperial.ac.uk

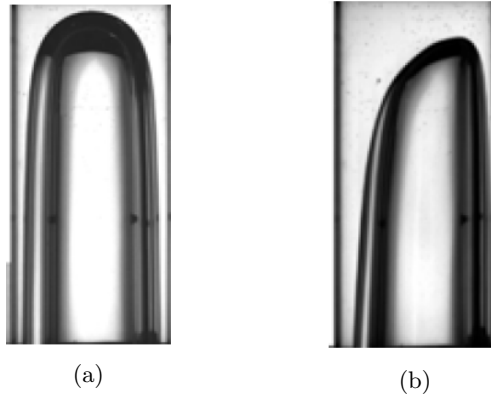


Figure 1: Taylor bubble shapes in a stagnant, (a), and downward-flowing liquid, (b), reproduced from Fabre & Figueroa-Espinoza (2014)

as experiments have confirmed the existence of a critical liquid velocity beyond which the bubble shape loses axisymmetry (Fabre & Figueroa-Espinoza 2014; Fershtman *et al.* 2017; Griffith & Wallis 1961; Martin 1976; Nicklin *et al.* 1962; Polonsky *et al.* 1999). An example of asymmetric bubble shapes in downward-flowing liquids is shown in Figure 1 in which it is seen that the bubble nose becomes distorted, and in an attempt to avoid the fast-moving fluid at the centre of the tube, the bubble moves closer to the tube wall (Nicklin *et al.* 1962), rising faster than it would have done had it remained axisymmetric (Martin 1976; Polonsky *et al.* 1999). It was also noted by Martin (1976) that for a downward-flowing liquid, a stable axisymmetric Taylor bubble can only be observed in tubes where surface tension effects are dominant, which is typical of small diameter tubes characterised by low Eötvös numbers; furthermore, the absolute value of the downward liquid velocity at which a bubble loses its axisymmetry decreases with increasing tube diameter.

Motivated by the aforementioned observations, Lu & Prosperetti (2006) carried out a linear stability analysis of a Taylor bubble moving in a downward-flowing liquid using potential flow theory and with negligible surface tension. They demonstrated that an axisymmetric Taylor bubble rising in a liquid with a laminar velocity profile subjected to irrotational perturbations becomes unstable beyond a critical negative liquid velocity. Following on from the theoretical investigation of Lu & Prosperetti (2006) and the numerical simulation of Figueroa-Espinoza & Fabre (2011), Fabre & Figueroa-Espinoza (2014) performed experimental investigations in tubes of diameters 20, 40, and 80 mm, complemented by numerical simulations using the boundary element method of Ha Ngoc & Fabre (2006). They showed that the radius of curvature of the bubble nose plays a key role in the stability of the Taylor bubble and that the onset of instability is dependent on the Eötvös number.

In this paper, we examine the stability of an axisymmetric steadily moving Taylor bubble in stagnant and flowing liquids, with particular attention given to the transition of the bubble shape from symmetric to asymmetric. To the best of our knowledge, the study of Lu & Prosperetti (2006) represents the first attempt in the literature to understand the mechanism governing this transition using linear theory. However, experimental studies (Fabre & Figueroa-Espinoza 2014) have shown that the onset of the instability is dependent on surface tension and by neglecting it, Lu & Prosperetti (2006) overestimate this onset. Moreover, existing studies of this transition have focused on the

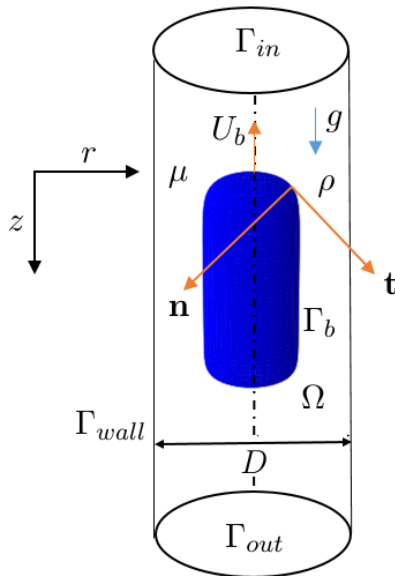


Figure 2: Three-dimensional axisymmetric Taylor bubble moving with a steady speed U_b through a liquid that is either stagnant or flowing (upwards or downwards) in a vertically-aligned tube of diameter D .

inertia-dominated regime, necessitating the need for investigating the parameter spaces where both viscous and surface tension effects are important. Thus, we carry out a linear stability analysis to understand how the forces acting on the bubble, characterised by the dimensionless inverse viscosity, Eötvös, and Froude numbers (the latter being based on the centreline liquid velocity) affect the loss of bubble axisymmetry. In addition, an energy budget analysis is carried out to determine the dominant, perturbation energy-producing terms that drive the instability. In a companion paper to the present work by Abubakar & Matar (2021), we computed the steady state solutions for an axisymmetric Taylor bubble rising steadily in stagnant and flowing liquids for different values of the aforementioned dimensionless parameters. These solutions serve as the base states for the linear stability analysis carried out herein. We relate the conclusions drawn from the steady state analysis by Abubakar & Matar (2021) to the mechanisms governing the instability.

The rest of this paper is organised as follows. In Section 2, we provide details of the governing equations, weak formulation, normal modes analysis, and validation of the numerical technique used to carry out the computations. A discussion of the results of the linear stability, and of the energy budget analyses is provided in Sections 3 and 4, respectively. Finally, in Section 5, concluding remarks and perspectives for future research on remaining open questions related to Taylor bubble motion are provided.

2. Problem formulation

2.1. Governing equations and boundary conditions

We consider a situation in which the two-dimensional axisymmetric steady state solution is revolved in the azimuthal direction to form a three-dimensional Taylor bubble, as shown in Figure 2. Here, we have adopted a cylindrical polar coordinate system (r, θ, z) in which r , θ , and z denote the radial, azimuthal, and axial coordinates, respectively. In

the steady state analysis of Abubakar & Matar (2021), the density, ρ_g , and viscosity, μ_g , of the gas phase are assumed to be very small compared to their liquid counterparts, ρ and μ , respectively. Hence, the dynamics in the gas phase is approximated by a constant pressure P_b , its influence being restricted to the interface separating the phases designated by Γ_b , and, consequently, only the liquid flow field and the P_b need to be determined.

The flow is governed by the Navier-Stokes and continuity equations which are non-dimensionalised by the characteristic length, velocity, and pressure scales, D , \sqrt{gD} , and $\rho g D$, respectively, where D is the tube diameter, and g is the gravitational acceleration. These equations are cast in a frame-of-reference translating with the velocity of the steadily-rising bubble nose $\mathbf{u}_b = -U_b \mathbf{i}_z$, in which U_b is the constant rise speed, and given by

$$\frac{\partial \mathbf{u}}{\partial t} + (\mathbf{u} \cdot \nabla) \mathbf{u} - \nabla \cdot \mathbf{T} = \mathbf{0}, \quad \text{in} \quad \Omega(t) \quad (2.1)$$

$$\nabla \cdot \mathbf{u} = 0, \quad \text{in} \quad \Omega(t) \quad (2.2)$$

where Ω denotes the domain of interest, $\mathbf{u} = (u_r, u_\theta, u_z)$ where u_r , u_θ , and u_z are the components of the liquid velocity vector in the moving frame-of-reference \mathbf{u} in the r , θ , and z directions, respectively, and t denotes time; \mathbf{T} is the total stress tensor given by

$$\mathbf{T} = -p\mathbf{I} + 2Nf^{-1}\mathbf{E}(\mathbf{u}), \quad (2.3)$$

in which p represents the dynamic pressure, $\mathbf{E} = (\nabla \mathbf{u} + \nabla \mathbf{u}^T)/2$ is the rate of deformation tensor, and $\nabla = \mathbf{i}_r \frac{\partial}{\partial r} + \mathbf{i}_\theta \frac{1}{r} \frac{\partial}{\partial \theta} + \mathbf{i}_z \frac{\partial}{\partial z}$ is the gradient operator in cylindrical polar coordinates where \mathbf{i}_r , \mathbf{i}_θ , and \mathbf{i}_z are the unit vectors in the radial, azimuthal, and axial directions, respectively, and \mathbf{I} is the unit tensor. In equation \mathbf{T} , the inverse viscosity number Nf is defined as follows

$$Nf = \frac{\rho (gD^3)^{\frac{1}{2}}}{\mu}. \quad (2.4)$$

The boundary of the domain, Γ , is divided into Γ_{in} , Γ_{out} , Γ_{wall} , and Γ_b as shown in Figure 2, with the subscripts ‘in’, ‘out’, ‘wall’, and ‘b’ representing the inlet, outlet, wall, and bubble boundaries, respectively. At the wall, no-slip and no-penetration boundary conditions are imposed:

$$\mathbf{u} = -\mathbf{u}_b \quad \text{on} \quad \Gamma_{wall}. \quad (2.5)$$

At the inlet, prescribed values, \mathbf{u}_{in} , are specified for the velocity components:

$$\mathbf{u} = \mathbf{u}_{in} - \mathbf{u}_b \quad \text{on} \quad \Gamma_{in}. \quad (2.6)$$

At the domain outlet, we impose the following conditions:

$$\mathbf{n} \cdot \mathbf{T} \cdot \mathbf{n} = 0, \quad (2.7a)$$

$$(\mathbf{I} - \mathbf{n} \otimes \mathbf{n}) \cdot \mathbf{u} = \mathbf{0}, \quad (2.7b)$$

where \mathbf{n} is the unit normal vector to the boundary. Finally, at the interface Γ_b , we set

$$\mathbf{n} \cdot \mathbf{T} \cdot \mathbf{n} + P_b - z - Eo^{-1}\kappa = 0, \quad (2.8)$$

$$\mathbf{n} \cdot \mathbf{T} \times \mathbf{n} = \mathbf{0}, \quad (2.9)$$

$$\frac{d\mathbf{r}_b}{dt} \cdot \mathbf{n} - \mathbf{u} \cdot \mathbf{n} = 0, \quad (2.10)$$

where κ is the curvature of the interface, $\mathbf{r}_b(t)$ represents the position vector of all the points on the portion of the boundary that corresponds to the interface Γ_b , and Eo is the dimensionless Eötvös number expressed by

$$Eo = \frac{\rho g D^2}{\gamma}, \quad (2.11)$$

in which γ denotes the (constant) surface tension. Equations (2.8)-(2.10) correspond to the normal stress, tangential stress, and kinematic boundary conditions, respectively. Note that gravity appears in (2.8) as z because the hydrostatic component of the pressure has been subtracted from the total pressure, leaving only the hydrodynamic part.

2.2. Weak forms and perturbation equations

We begin the model development from the weak forms of the momentum and continuity equations (see appendix A):

$$\int_V \left\{ \frac{\partial \mathbf{u}}{\partial t} \cdot \Phi + [(\mathbf{u} \cdot \nabla) \mathbf{u}] \cdot \Phi + 2Nf^{-1} \mathbf{E}(\mathbf{u}) : \mathbf{E}(\Phi) - p(\nabla \cdot \Phi) \right\} dV, \\ - \int_{A_b} \{ [Eo^{-1} \kappa + z - P_b] \mathbf{n} \cdot \Phi \} dA_b = 0, \quad (2.12)$$

$$\int_V \{ (\nabla \cdot \mathbf{u}) \varphi \} dV = 0. \quad (2.13)$$

Also, we have the weak form of the kinematic boundary condition:

$$\int_{A_b} \left\{ \left[\frac{d\mathbf{r}_b}{dt} \cdot \mathbf{n} - \mathbf{u} \cdot \mathbf{n} \right] \xi \right\} dA_b = 0. \quad (2.14)$$

In equations (2.12)-(2.14), Φ , φ , and ξ denote the test functions for the velocity vector, pressure, and interface deformation magnitude, respectively.

Similar to domain perturbation, we assume that the three-dimensional base flow domain is perturbed by the addition of infinitesimal deformation field $\tilde{\mathbf{x}}$ to its position vector and that equations (2.12)-(2.14) are valid on the three-dimensional perturbed domain. A similar approach has been adopted in the three-dimensional linear stability analysis of coating flow problems by Carvalho & Scriven (1999); Christodoulou & Scriven (1988). The perturbed three-dimensional domain can then be linearised around the base state three-dimensional axisymmetric domain, the deformation field restricted to the interface, just as it is expected in the classical linear stability approach; finally, the linearisation of the perturbed flow field variables about the base state solution is carried out. This approach to the derivation of the linear stability model can be seen as an extension of the total linearisation method used in solving two-dimensional viscous free boundary problems (Cuvelier & Schulkes 1990; Kruyt *et al.* 1988) to three dimensions.

Let the position vector of the perturbed domain be written as

$$\mathbf{r} = \mathbf{r}^0 + \epsilon \tilde{\mathbf{x}}, \quad (2.15)$$

where $\mathbf{r}^0 = (r^0, \theta^0, z^0)$ represents the position vector of the unperturbed three-dimensional base flow domain, $\tilde{\mathbf{x}} = (\tilde{x}_r, \tilde{x}_\theta, \tilde{x}_z)$ is a deformation field defined over the entire base flow domain, and $\epsilon \ll 1$ to signify the infinitesimally small nature of the applied perturbations. The linearised elemental volume of the perturbed three-dimensional

domain is given as (Cairncross *et al.* 2000; Carvalho & Scriven 1999)

$$\begin{aligned} dV &= r dr d\theta dz = (1 + \nabla \cdot \tilde{\mathbf{x}}) r^0 dr^0 d\theta^0 dz^0 \\ &= (1 + \nabla \cdot \tilde{\mathbf{x}}) d\Omega^0 d\theta^0; \end{aligned} \quad (2.16)$$

thus, we can relate the elemental volume in the perturbed three-dimensional domain to the base flow two-dimensional axisymmetric domain, $d\Omega^0 = r^0 dr^0 dz^0$. Similarly, an elemental area on the perturbed interface in the three-dimensional domain, dA_b , can be related to base flow length of arc, Γ_b^0 in the two-dimensional axisymmetric domain:

$$dA_b = (1 + \nabla_s \cdot \tilde{\mathbf{x}}) d\Gamma_b^0 d\theta^0, \quad (2.17)$$

where ∇_s is the surface gradient operator; the interface terms can be linearised as follows

$$\mathbf{n} = \mathbf{n}^0 + \epsilon \tilde{\mathbf{n}}, \quad (2.18a)$$

$$\kappa = \kappa^0 + \epsilon \tilde{\kappa}, \quad (2.18b)$$

$$\Phi = \Phi + \epsilon (\tilde{\mathbf{x}} \cdot \nabla) \Phi, \quad (2.18c)$$

$$\mathbf{u} = \mathbf{u} + \epsilon (\tilde{\mathbf{x}} \cdot \nabla) \mathbf{u}; \quad (2.18d)$$

here, \mathbf{n}^0 and κ^0 are the base state interface normal vector and curvature, and $\tilde{\mathbf{n}}$ and $\tilde{\kappa}$ represent the normal vector and curvature perturbations, respectively (see Appendix B):

$$\tilde{\mathbf{n}} = -\mathbf{t}^0 \left(\mathbf{n}^0 \cdot \frac{d\tilde{\mathbf{x}}}{ds^0} \right) - \frac{\mathbf{n}^0}{r^0} \cdot \frac{\partial \tilde{\mathbf{x}}}{\partial \theta^0}, \mathbf{i}_\theta \quad (2.19)$$

$$\begin{aligned} \tilde{\kappa} &= \frac{1}{r^0} \frac{d}{ds^0} \left[r^0 \left(\mathbf{n}^0 \cdot \frac{d\tilde{\mathbf{x}}}{ds^0} \right) \right] + 2 \left(\mathbf{t}^0 \cdot \frac{d\tilde{\mathbf{x}}}{ds^0} \right) \left(\mathbf{t}^0 \cdot \frac{d\mathbf{n}^0}{ds^0} \right) \\ &\quad + \frac{\mathbf{n}^0}{r^{02}} \cdot \frac{\partial^2 \tilde{\mathbf{x}}}{\partial \theta^{02}} + \frac{\tilde{x}_r n_r^0}{r^{02}} - \frac{d\mathbf{n}^0}{ds^0} \cdot \frac{d\tilde{\mathbf{x}}}{ds^0}, \end{aligned} \quad (2.20)$$

where $\frac{d}{ds^0} = \mathbf{t} \cdot \nabla$ is the derivative along the arc length s on the base state interface. Substitution into equations (2.12)-(2.14) of equations (2.15)-(2.18), together with the flow field perturbations

$$\mathbf{u} = \mathbf{u}^0 + \epsilon \tilde{\mathbf{u}}, \quad (2.21a)$$

$$p = p^0 + \epsilon \tilde{p}, \quad (2.21b)$$

followed by neglecting all terms of order ϵ^2 respectively yields the following leading order momentum, continuity, and kinematic condition equations

$$\begin{aligned} &\int_0^{2\pi} \left\{ \int_{\Omega^0} \{ [(\mathbf{u}^0 \cdot \nabla) \mathbf{u}^0] \cdot \Phi + 2Nf^{-1} \mathbf{E}(\mathbf{u}^0) : \mathbf{E}(\Phi) - p^0 (\nabla \cdot \Phi) \} d\Omega^0 \right. \\ &\quad \left. - \int_{\Gamma_b^0} \{ [Eo^{-1} \kappa^0 + z^0 - P_b^0] \mathbf{n}^0 \cdot \Phi \} d\Gamma_b^0 \right\} d\theta^0, \end{aligned} \quad (2.22)$$

$$\int_0^{2\pi} \int_{\Omega^0} \{ (\nabla \cdot \mathbf{u}^0) \varphi \} [1 + \nabla \cdot \tilde{\mathbf{x}}] d\Omega^0 d\theta^0, \quad (2.23)$$

$$\int_0^{2\pi} \int_{\Gamma_b^0} \left\{ \left[\frac{d\mathbf{r}_b^0}{dt} \cdot \mathbf{n}^0 - \mathbf{u}^0 \cdot \mathbf{n}^0 \right] \xi \right\} [1 + \nabla_s \cdot \tilde{\mathbf{x}}] d\Gamma_b^0 d\theta^0. \quad (2.24)$$

It is also possible to write the following equations at $O(\epsilon)$ to yield equations that feature the perturbation variables: the momentum conservation equation,

$$\begin{aligned} & \int_0^{2\pi} \int_{\Omega^0} \left\{ \frac{\partial \tilde{\mathbf{u}}}{\partial t} \cdot \Phi + [(\mathbf{u}^0 \cdot \nabla) \tilde{\mathbf{u}} + (\tilde{\mathbf{u}} \cdot \nabla) \mathbf{u}^0] \cdot \Phi + 2N f^{-1} \mathbf{E}(\tilde{\mathbf{u}}) : \mathbf{E}(\Phi) \right\} d\Omega^0 d\theta^0 \\ & - \int_0^{2\pi} \int_{\Omega^0} \{ \tilde{p}(\nabla \cdot \Phi) \} d\Omega^0 d\theta^0 \\ & - \int_0^{2\pi} \int_{\Gamma_b^0} \{ [E o^{-1} \tilde{\kappa} + \tilde{z}] \mathbf{n}^0 \cdot \Phi \} d\Gamma_b^0 d\theta^0 \\ & + \int_0^{2\pi} \int_{\Gamma_b^0} \tilde{\mathbf{x}} \cdot \mathbf{n}^0 \{ [(\mathbf{u}^0 \cdot \nabla) \mathbf{u}^0] \cdot \Phi + 2N f^{-1} \mathbf{E}(\mathbf{u}^0) : \mathbf{E}(\Phi) - p^0(\nabla \cdot \Phi) \} d\Gamma_b^0 d\theta^0 \\ & - \int_0^{2\pi} \int_{\Gamma_b^0} \{ [E o^{-1} \kappa^0 + z^0 - P_b^0] [\tilde{\mathbf{n}} \cdot \Phi + [(\tilde{\mathbf{x}} \cdot \nabla) \Phi] \cdot \mathbf{n}^0 + (\nabla_s \cdot \tilde{\mathbf{x}}) \mathbf{n}^0 \cdot \Phi] \} d\Gamma_b^0 d\theta^0 \\ & = 0, \end{aligned} \quad (2.25)$$

where \mathbf{u}^0 , p^0 , and P_b^0 represent the base flow solutions for the variables; and $\tilde{\mathbf{u}}$ and \tilde{p} denote the perturbations to the flow field variables, and the last two lines of (2.25) are due to the linearisation of the domain and boundary terms of equation (2.12) where we have used Gauss's divergence theorem to restrict the deformation to the interface as it is expected in classical linear stability formulation; the continuity equation,

$$\int_0^{2\pi} \int_{\Omega^0} \{ (\nabla \cdot \tilde{\mathbf{u}}) \varphi \} d\Omega^0 d\theta^0 = 0, \quad (2.26)$$

and the kinematic condition:

$$\int_0^{2\pi} \int_{\Gamma_b^0} \left\{ \left[\frac{d\tilde{\mathbf{x}}}{dt} \cdot \mathbf{n}^0 - \tilde{\mathbf{u}} \cdot \mathbf{n}^0 - \mathbf{u}^0 \cdot \tilde{\mathbf{n}} - [(\tilde{\mathbf{x}} \cdot \nabla) \mathbf{u}^0] \cdot \mathbf{n}^0 \right] \xi \right\} d\Gamma_b^0 d\theta^0 = 0. \quad (2.27)$$

Simplifying equations (2.25)-(2.27) further by substituting for $\tilde{\mathbf{n}}$ and $\tilde{\kappa}$ using equations (2.19) and (2.20), respectively, and taking the deformation field to be of the form $\tilde{\mathbf{x}} = \tilde{h} \mathbf{n}^0$, since the deformation has been restricted to the interface and making use of the relations

$$\mathbf{u}^0 = (\mathbf{u}^0 \cdot \mathbf{n}^0) \mathbf{n}^0 + (\mathbf{u}^0 \cdot \mathbf{t}^0) \mathbf{t}^0, \quad (2.28a)$$

$$\nabla = (\mathbf{I} - \mathbf{n}^0 \otimes \mathbf{n}^0) \cdot \nabla + (\mathbf{n}^0 \otimes \mathbf{n}^0) \cdot \nabla, \quad (2.28b)$$

equations (2.25)-(2.27), after some algebra, can be expressed as follows

$$\begin{aligned}
& \int_0^{2\pi} \int_{\Omega^0} \left\{ \frac{\partial \tilde{\mathbf{u}}}{\partial t} \cdot \Phi + [(\mathbf{u}^0 \cdot \nabla) \tilde{\mathbf{u}} + (\tilde{\mathbf{u}} \cdot \nabla) \mathbf{u}^0] \cdot \Phi + 2Nf^{-1} \mathbf{E}(\tilde{\mathbf{u}}) : \mathbf{E}(\Phi) \right\} d\Omega^0 d\theta \\
& - \int_0^{2\pi} \int_{\Omega^0} \{ \tilde{p}(\nabla \cdot \Phi) \} d\Omega^0 d\theta \\
& - \int_0^{2\pi} \int_{\Gamma_b^0} Eo^{-1} \left\{ -\frac{d\tilde{h}}{ds} \left[\mathbf{n} \cdot \frac{d\Phi}{ds} - \kappa_a(\mathbf{t} \cdot \Phi) \right] + \left[\tilde{h}(\kappa_a^2 + \kappa_b^2) + \frac{1}{r^2} \frac{\partial^2 \tilde{h}}{\partial \theta^2} \right] \mathbf{n} \cdot \Phi \right\} d\Gamma_b^0 d\theta \\
& - \int_0^{2\pi} \int_{\Gamma_b^0} \{ \tilde{h} n_z(\mathbf{n} \cdot \Phi) \} d\Gamma_b^0 d\theta \\
& + \int_0^{2\pi} \int_{\Gamma_b^0} \tilde{h} \left\{ (\mathbf{u}^0 \cdot \mathbf{t}) \left[\frac{d\mathbf{u}^0}{ds} \cdot \Phi \right] + \left[-p^0 + 2Nf^{-1} \left(\mathbf{t} \cdot \frac{d\mathbf{u}^0}{ds} \right) \right] \left(\mathbf{t} \cdot \frac{d\Phi}{ds} \right) \right. \\
& + \left. \left[-p^0 + 2Nf^{-1} \frac{u_r^0}{r} \right] \left(\frac{\Phi_r}{r} + \frac{1}{r} \frac{\partial \Phi_\theta}{\partial \theta} \right) \right\} d\Gamma_b^0 d\theta \\
& + \int_0^{2\pi} \int_{\Gamma_b^0} \left\{ [Eo^{-1} \kappa + z - P_b^0] \left[(\mathbf{t} \cdot \Phi) \frac{d\tilde{h}}{ds} + \frac{\Phi_\theta}{r} \frac{\partial \tilde{h}}{\partial \theta} + \tilde{h} \kappa(\mathbf{n} \cdot \Phi) \right] \right\} d\Gamma_b^0 d\theta = 0,
\end{aligned} \tag{2.29}$$

$$\int_0^{2\pi} \int_{\Omega^0} \{ (\nabla \cdot \tilde{\mathbf{u}}) \varphi \} d\Omega d\theta = 0, \tag{2.30}$$

$$\int_0^{2\pi} \int_{\Gamma_b^0} \left\{ \left[\frac{d\tilde{h}}{dt} - \tilde{\mathbf{u}} \cdot \mathbf{n} + (\mathbf{u}^0 \cdot \mathbf{t}) \frac{d\tilde{h}}{ds} - \tilde{h} \left(\frac{d\mathbf{u}^0}{dn} \cdot \mathbf{n} \right) \right] \xi \right\} d\Gamma_b^0 d\theta = 0, \tag{2.31}$$

where $\frac{d}{dn} = (\mathbf{n} \cdot \nabla)$ is the derivative in the normal direction. In equations (2.29)-(2.31), we have suppressed the use of the superscript '0' to designate base state quantities for the unit tangent and normal vectors for the sake of brevity.

2.3. Normal modes

Let us take the following normal mode forms for the perturbation variables:

$$\tilde{\mathbf{u}}(r, \theta, z, t) = \hat{\mathbf{u}}(r, z) e^{(im\theta + \beta t)}, \tag{2.32a}$$

$$\tilde{p}(r, \theta, z, t) = \hat{p}(r, z) e^{(im\theta + \beta t)}, \tag{2.32b}$$

$$\tilde{h}(s, \theta, t) = \hat{h}(s) e^{(im\theta + \beta t)}, \tag{2.32c}$$

and their corresponding test functions as

$$\Phi(r, \theta, z) = \bar{\Phi}(r, z) e^{(-im\theta)}, \tag{2.33a}$$

$$\varphi(r, \theta, z) = \bar{\varphi}(r, z) e^{(-im\theta)}, \tag{2.33b}$$

$$\xi(s, \theta) = \bar{\xi}(s) e^{(-im\theta)}, \tag{2.33c}$$

where $\hat{\mathbf{u}}$, \hat{p} , and \hat{h} are complex functions of space representing the amplitude of the velocity, pressure, and interface deformation perturbations, respectively; m is a dimensionless (integer) wave number in the azimuthal direction θ ; $\beta = \beta_R + i\beta_I$ is the complex growth rate which can be decomposed into its real β_R and imaginary β_I parts denoting the temporal growth rate and frequency, respectively: if β_R is positive

(negative), the disturbance grows (decays) exponentially in time and the base flow is linearly unstable (stable); if β_R is zero, the disturbance is neutrally stable. Substituting equations (2.32) and (2.33) into (2.29)-(2.31), separating the momentum equation into its components, yields the following equations governing the normal mode evolution of the perturbations as a function of Nf , EO , U_m , and m :

$$\begin{aligned}
& \int_{\Omega^0} \left\{ \beta \hat{u}_r \bar{\Phi}_r + \left[\hat{u}_r \frac{\partial u_r^0}{\partial r} + \hat{u}_z \frac{\partial u_r^0}{\partial z} + u_r^0 \frac{\partial \hat{u}_r}{\partial r} + u_z^0 \frac{\partial \hat{u}_r}{\partial z} \right] \bar{\Phi}_r + Nf^{-1} \left[2 \frac{\partial \hat{u}_r}{\partial r} \frac{\partial \bar{\Phi}_r}{\partial r} \right. \right. \\
& \quad \left. \left. + (2 + m^2) \frac{\hat{u}_r \bar{\Phi}_r}{r^2} + 3im \frac{\hat{u}_\theta \bar{\Phi}_r}{r^2} - im \frac{\bar{\Phi}_r}{r} \frac{\partial \hat{u}_\theta}{\partial r} + \frac{\partial \bar{\Phi}_r}{\partial z} \left(\frac{\partial \hat{u}_r}{\partial z} + \frac{\partial \hat{u}_z}{\partial r} \right) \right] \right. \\
& \quad \left. - \hat{p} \left(\frac{\partial \bar{\Phi}_r}{\partial r} + \frac{\bar{\Phi}_r}{r} \right) \right\} d\Omega^0 \\
& - \int_{\Gamma_b^0} EO^{-1} \left\{ -\frac{d\hat{h}}{ds} \left[n_r \frac{d\bar{\Phi}_r}{ds} - \kappa_a (t_r \bar{\Phi}_r) \right] + \hat{h} \left[\kappa_a^2 + \kappa_b^2 - \frac{m^2}{r^2} \right] n_r \bar{\Phi}_r \right\} d\Gamma_b^0 \\
& - \int_{\Gamma_b^0} \left\{ \hat{h} n_z (n_r \bar{\Phi}_r) \right\} d\Gamma_b^0 \\
& + \int_{\Gamma_b^0} \hat{h} \left\{ (u_r^0 t_r) \left[\frac{du_r^0}{ds} \bar{\Phi}_r \right] + \left[-p^0 + 2Nf^{-1} \left(t_r \frac{du_r^0}{ds} \right) \right] \left(t_r \frac{d\bar{\Phi}_r}{ds} \right) \right. \\
& \quad \left. + \left[-p^0 + 2Nf^{-1} \frac{u_r^0}{r} \right] \left(\frac{\bar{\Phi}_r}{r} \right) \right\} d\Gamma_b^0 \\
& + \int_{\Gamma_b^0} \left\{ [EO^{-1} \kappa + z - P_b^0] \left[(t_r \bar{\Phi}_r) \frac{d\hat{h}}{ds} + \hat{h} \kappa (n_r \bar{\Phi}_r) \right] \right\} d\Gamma_b^0 = 0, \tag{2.34}
\end{aligned}$$

$$\begin{aligned}
& \int_{\Omega^0} \left\{ \beta \hat{u}_\theta \bar{\Phi}_\theta + \left[u_r^0 \frac{\partial \hat{u}_\theta}{\partial r} + u_z^0 \frac{\partial \hat{u}_\theta}{\partial z} + \frac{u_r^0 \hat{u}_\theta}{r} \right] \bar{\Phi}_\theta + Nf^{-1} \left[(1 + 2m^2) \frac{\hat{u}_\theta \bar{\Phi}_\theta}{r^2} + \frac{\partial \hat{u}_\theta}{\partial z} \frac{\partial \bar{\Phi}_\theta}{\partial z} \right. \right. \\
& \quad \left. \left. + \frac{\partial \hat{u}_\theta}{\partial r} \frac{\partial \bar{\Phi}_\theta}{\partial r} - \left(\frac{\hat{u}_\theta}{r} \frac{\partial \bar{\Phi}_\theta}{\partial r} + \frac{\bar{\Phi}_\theta}{r} \frac{\partial \hat{u}_\theta}{\partial r} \right) + im \left(\frac{\hat{u}_r}{r} \frac{\partial \bar{\Phi}_\theta}{\partial r} + \frac{\hat{u}_z}{r} \frac{\partial \bar{\Phi}_\theta}{\partial z} \right) - 3im \frac{\hat{u}_r \bar{\Phi}_\theta}{r^2} \right] \right. \\
& \quad \left. - p \left(-im \frac{\bar{\Phi}_\theta}{r} \right) \right\} d\Omega^0 + \int_{\Gamma_b^0} \hat{h} \left\{ \left[-p^0 + 2Nf^{-1} \frac{u_r^0}{r} \right] \left(-im \frac{\bar{\Phi}_\theta}{r} \right) \right\} d\Gamma_b^0 \\
& + \int_{\Gamma_b^0} \left\{ \hat{h} [EO^{-1} \kappa + z - P_b^0] \left[im \frac{\bar{\Phi}_\theta}{r} \right] \right\} d\Gamma_b^0 = 0, \tag{2.35}
\end{aligned}$$

$$\begin{aligned}
& \int_{\Omega^0} \left\{ \beta \hat{u}_z \bar{\Phi}_z + \left[\hat{u}_r \frac{\partial u_z^0}{\partial r} + \hat{u}_z \frac{\partial u_z^0}{\partial z} + u_r^0 \frac{\partial \hat{u}_z}{\partial r} + u_z^0 \frac{\partial \hat{u}_z}{\partial z} \right] \bar{\Phi}_z + N f^{-1} \left[2 \frac{\partial \hat{u}_z}{\partial z} \frac{\partial \bar{\Phi}_z}{\partial z} + m^2 \frac{\hat{u}_z \bar{\Phi}_z}{r^2} \right. \right. \\
& \quad \left. \left. - im \frac{\bar{\Phi}_z}{r} \frac{\partial \hat{u}_\theta}{\partial z} + \frac{\partial \bar{\Phi}_z}{\partial r} \left(\frac{\partial \hat{u}_r}{\partial z} + \frac{\partial \hat{u}_z}{\partial r} \right) \right] - \hat{p} \left(\frac{\partial \bar{\Phi}_z}{\partial z} \right) \right\} d\Omega^0 \\
& - \int_{\Gamma_b^0} E o^{-1} \left\{ -\frac{d\hat{h}}{ds} \left[n_z \frac{d\bar{\Phi}_z}{ds} - \kappa_a (t_z \bar{\Phi}_z) \right] + \hat{h} \left[\kappa_a^2 + \kappa_b^2 - \frac{m^2}{r^2} \right] n_z \bar{\Phi}_z \right\} d\Gamma_b^0 \\
& - \int_{\Gamma_b^0} \left\{ \hat{h} n_z (n_z \bar{\Phi}_z) \right\} d\Gamma_b^0 \\
& + \int_{\Gamma_b^0} \hat{h} \left\{ (u_z^0 t_z) \left[\frac{du_z^0}{ds} \bar{\Phi}_z \right] + \left[-p^0 + 2N f^{-1} \left(t_z \frac{du_z^0}{ds} \right) \right] \left(t_z \frac{d\bar{\Phi}_z}{ds} \right) \right\} d\Gamma_b^0 \\
& + \int_{\Gamma_b^0} \left\{ [E o^{-1} \kappa + z - P_b^0] \left[(t_z \bar{\Phi}_z) \frac{d\hat{h}}{ds} + \hat{h} \kappa (n_z \bar{\Phi}_z) \right] \right\} d\Gamma_b^0 = 0, \tag{2.36}
\end{aligned}$$

$$\int_{\Omega^0} \left\{ \left[\frac{\partial \hat{u}_r}{\partial r} + \frac{\hat{u}_r}{r} - im \frac{\hat{u}_\theta}{r} + \frac{\partial \hat{u}_z}{\partial z} \right] \bar{\varphi} \right\} d\Omega^0 = 0, \tag{2.37}$$

$$\int_{\Gamma_b^0} \left\{ \left[\beta \hat{h} - \hat{\mathbf{u}} \cdot \mathbf{n} + (\mathbf{u}^0 \cdot \mathbf{t}) \frac{d\hat{h}}{ds} - \hat{h} \left(\frac{d\mathbf{u}^0}{dn} \cdot \mathbf{n} \right) \right] \bar{\xi} \right\} d\Gamma_b^0 = 0. \tag{2.38}$$

The combined finite element forms for the perturbations equations (2.34)-(2.38) can be recast as a generalised eigenvalue problem

$$\beta \mathbf{B} \mathbf{y} = \mathbf{J} \mathbf{y}, \tag{2.39}$$

with β being the eigenvalue, \mathbf{B} the mass matrix, \mathbf{y} the eigenfunctions, and \mathbf{J} the Jacobian matrix respectively given by

$$\mathbf{B} = \begin{bmatrix} \mathbf{B}_{r,r} & 0 & 0 & 0 & 0 \\ 0 & \mathbf{B}_{\theta,\theta} & 0 & 0 & 0 \\ 0 & 0 & \mathbf{B}_{z,z} & 0 & 0 \\ 0 & 0 & 0 & 0 & 0 \\ 0 & 0 & 0 & 0 & \mathbf{B}_h \end{bmatrix}, \quad \mathbf{y} = \begin{bmatrix} \hat{\mathbf{v}}_r \\ \hat{\mathbf{v}}_\theta \\ \hat{\mathbf{v}}_z \\ \hat{\mathbf{p}} \\ \hat{\mathbf{h}} \end{bmatrix},$$

$$\mathbf{J} = - \begin{bmatrix} (\mathbf{C}_{r,r} + \mathbf{K}_{r,r}) & \mathbf{K}_{r,\theta} & (\mathbf{C}_{r,z} + \mathbf{K}_{r,z}) & -\mathbf{Q}_r^T & \mathbf{M}_{r,h} \\ \mathbf{K}_{r,\theta}^T & (\mathbf{C}_{\theta,\theta} + \mathbf{K}_{\theta,\theta}) & \mathbf{K}_{z,\theta}^T & -\mathbf{Q}_\theta^T & \mathbf{M}_{\theta,h} \\ (\mathbf{C}_{z,r} + \mathbf{K}_{r,z}^T) & \mathbf{K}_{z,\theta} & (\mathbf{C}_{z,z} + \mathbf{K}_{z,z}) & -\mathbf{Q}_z^T & \mathbf{M}_{z,h} \\ -\mathbf{Q}_r & -\mathbf{Q}_\theta & -\mathbf{Q}_z & 0 & 0 \\ -\mathbf{X}_r & 0 & -\mathbf{X}_z & 0 & \mathbf{X}_h \end{bmatrix}$$

where $\mathbf{B}_{i,i} \quad \forall i = r, \theta, z$ are coefficient matrices for the i component of velocity in the i component of momentum equation. $\mathbf{C}_{i,j}$ and $\mathbf{K}_{i,j} \quad \forall i = r, \theta, z$ are the convective and viscous coefficient matrices for the j component of velocity in the i component of momentum equation, respectively. $\mathbf{M}_{i,h} \quad \forall i = r, \theta, z$ are coefficient matrices for interface deformation magnitude in the i component of momentum equation. $\mathbf{Q}_j \quad \forall j = r, \theta, z$ are coefficient matrices for the j component of velocity in the continuity equation, whose Hermitian transpose correspond to the coefficient matrices of pressure in the j component of momentum equation. $\mathbf{X}_j \quad \forall j = r, z$ are coefficient matrices for the j component of velocity in the kinematic boundary condition. \mathbf{B}_h and \mathbf{X}_h are the coefficient matrices of interface deformation magnitude in the kinematic boundary condition for the mass

and Jacobian matrices, respectively. The operator $(\cdot)^T$ denotes the Hermitian transpose. The full expressions for the coefficient matrices in the mass and Jacobian matrices are given in Appendix C.

The boundary conditions at the inlet, wall, and outlet reduce to the following conditions on the perturbations:

$$\hat{\mathbf{u}} = \mathbf{0} \quad \text{on} \quad \Gamma_{in}^0 \quad \text{and} \quad \Gamma_{wall}^0, \quad (2.40)$$

$$\mathbf{n} \cdot \hat{\mathbf{T}} \cdot \mathbf{n} = 0 \quad \text{and} \quad (\mathbf{I} - \mathbf{n} \otimes \mathbf{n}) \cdot \hat{\mathbf{u}} = 0 \quad \text{on} \quad \Gamma_{out}^0, \quad (2.41)$$

where the tensor $\hat{\mathbf{T}}$ is expressed by

$$\hat{\mathbf{T}} = -\hat{p} + 2Nf^{-1}\hat{\mathbf{E}}(\hat{\mathbf{u}}); \quad \hat{\mathbf{E}}(\hat{\mathbf{u}}) = \frac{1}{2} [\nabla \hat{\mathbf{u}} + \nabla \hat{\mathbf{u}}^T].$$

We stress that while it is customary to impose additional conditions along the axis of symmetry Γ_{sym}^0 , we did not apply any such conditions in this case because the model equations were written around the perturbed three-dimensional domain and then linearised before integrating out the θ dependence.

2.4. Numerical method and validation

2.4.1. Linear algebra

The linear stability of the steady state solutions as a parametric function of the system dimensionless groups is determined by solving a generalized, asymmetric matrix eigenvalue problem given by equation (2.39). The asymmetric nature of the problem, as can be seen by inspection of the Jacobian matrix, is due to the convective and interface deformation contributions to the matrix. In addition, it can also be seen that the mass matrix is singular, with several rows having identically zero entries, which can be attributed to the absence of time derivative terms in the continuity equation and though not obvious, due to the requirement that the perturbation vectors satisfy homogeneous essential boundary conditions (Carvalho & Scriven 1999; Natarajan 1992). The implication of having singularity in the mass matrix is that the number of true eigenvalues is smaller than the dimension of the problem, with the number of missing eigenvalues equal to the number of algebraic equations having identically zero row in the matrix (Carvalho & Scriven 1999). We carry out a shift-and-invert transformation (Christodoulou & Scriven 1988) to map these missing, or so-called ‘infinite’, eigenvalues to zero wherein the original problem is transformed to

$$(\mathbf{J} - v\mathbf{B})^{-1} \mathbf{B}\mathbf{y} = \tau\mathbf{y}, \quad (2.42)$$

where the shift v is a complex constant, τ is the eigenvalue of the new problem and is related to the eigenvalue of the original problem β by

$$\tau = \frac{1}{(\beta - v)}. \quad (2.43)$$

We solve this eigenvalue problem by using an iterative Arnoldi method available in ARPACK (Lehoucq *et al.* 1997), which can be called within FreeFem++, using the standard *Taylor-Hood* element for the flow field variables and piecewise quadratic element for interface deformation magnitude as in the steady state simulations. The accuracy of the converged leading eigenvalue is confirmed by ensuring that the residual $|\mathbf{J}\mathbf{y} - \beta\mathbf{B}\mathbf{y}|$ is always less than 1×10^{-10} .

2.4.2. Validation

We test the validity of our theoretical and numerical procedure by examining the stability of a spherical bubble of fixed volume in a stagnant liquid with negligible gravitational and boundary effects. The bubble is stable under these conditions and its motion is governed by an analytical solution (Miller & Scriven 1968; Prosperetti 1980). We compare our numerical results for the eigenvalues with this solution given in Prosperetti (1980) for small amplitude normal mode perturbations. The characteristic scales used for the non-dimensionalisation of space, velocity, and pressure in the governing equations are R , $\sqrt{\gamma/(\rho R)}$, and γ/R , respectively, where R is the bubble radius, so that the validation problem is parameterised by the Ohnesorge number, $Oh\mu/\sqrt{\rho R\gamma}$.

Based on the scaling above, the dimensionless form of the characteristic equation for the bubble oscillations reads (Prosperetti 1980)

$$\begin{aligned} & \left[\mathcal{H}_{m-\frac{1}{2}}^{(1)}(X^*) \right] \beta^2 + Oh \left[4m(m+2)^2 - 2(m+2)(2m+1)(\mathcal{H}_{m-\frac{1}{2}}^{(1)}(X^*) + 2) \right] \beta \\ & + (m+1)(m-1)(m+2)(\mathcal{H}_{m-\frac{1}{2}}^{(1)}(X^*) + 2) = 0, \end{aligned} \quad (2.44)$$

where X^* is a rescaled growth rate, and $\mathcal{H}_j^{(1)}(X^*)$ is a Hankel function of the first kind:

$$X^* = \left[\frac{\beta}{Oh} \right]^{\frac{1}{2}}, \quad \text{and} \quad \mathcal{H}_j^{(1)}(X^*) = \frac{X^* H_{j+1}^{(1)}(X^*)}{H_j^{(1)}(X^*)}. \quad (2.45)$$

For a fixed value of Oh , we solve iteratively for β . The initial guess used is the solution to the following equation (Prosperetti 1980)

$$\beta^2 - 2Oh[(m+2)(2m+1)]\beta + (m+1)(m-1)(m+2) = 0. \quad (2.46)$$

Once the solution for the first eigenvalue is obtained, we use the associated X^* for the previous Oh as the initial guess for the next value of Oh . We implemented the solution steps in MATLAB and generated the analytical solution for $0 \leq Oh \leq 1$.

At steady state, in the absence of gravity and since the liquid surrounding the bubble is stagnant ($\mathbf{u} = 0$), the governing equations reduce to

$$\nabla p = 0, \quad (2.47)$$

and the normal stress boundary condition to

$$-p + P_b = \kappa \text{ on } \Gamma_b. \quad (2.48)$$

Equation (2.47) implies that pressure field in the liquid phase surrounding the bubble is a constant, P_a , so that the bubble pressure becomes

$$P_b = \kappa + P_a \quad \text{on } \Gamma_b. \quad (2.49)$$

For the linear stability analysis, the value of P_a was set to zero without loss of generality.

We solve the modified forms of the perturbation equations (2.34)-(2.38) using the base state solutions computed as set out above. Figures 3a and 3b respectively show excellent agreement between the real and imaginary parts of the eigenvalues computed and the analytical solution of (2.44) as a function of the Ohnesorge number for four different azimuthal wavenumbers.

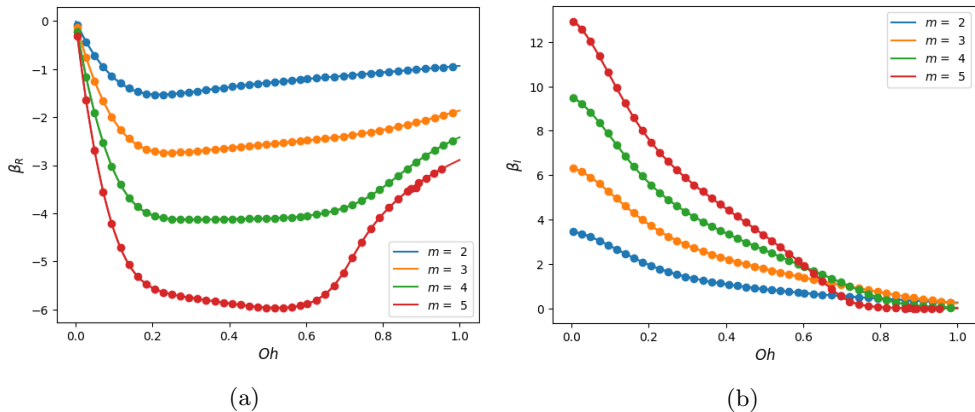


Figure 3: Validation of the theoretical and numerical procedure for an oscillating bubble in the absence of gravitational and boundary effects. Comparison between the amplification rates, (a), and oscillation frequencies, (b), from the analytical solution given by equation (2.44) (coloured continuous solid line) and our numerically-generated growth rates (coloured markers), for modes $m = 2, 3, 4$ and 5 .

3. Linear stability results

In this section, we provide a discussion of the linear stability results starting with the dependence of the growth rate β_R obtained from the leading eigenvalues associated primarily with the first two modes, $m = 1$ and $m = 2$, as a parametric function of Nf , EO , and U_m . The asymmetric bubble shape near instability onset, associated with the most dangerous linear mode, is also discussed, and a stability map is plotted which clearly demarcates the stability boundary as a function of the system parameters.

3.1. Dominant modes of instability

The linear stability of axisymmetric steady states associated with $40 \leq Nf \leq 100$ and $20 \leq EO \leq 300$ was investigated for downward liquid flow characterised by $U_m < 0$; these base states had been computed and reported in the companion paper to the present work by Abubakar & Matar (2021). In Figure 4, we show the dependence of the growth rate β_R on U_m for modes $m = 1$, $m = 2$, and $m = 3$ for $Nf = 40, 60, 80, 100$, and $EO = 20, 180, 300$. For all the cases shown in this figure, it is evident that $m = 1$ is the most unstable mode, which corresponds to a deflection of the bubble away from the axis of symmetry and occurs over a well-defined range of negative U_m values, ΔU_m , for which $\beta_R > 0$ indicating the presence of a linear instability. For sufficiently large EO and Nf , the $m = 2$ is also unstable, though it remains sub-dominant to the $m = 1$ mode, as illustrated in Figure 4(1), for instance, for the $Nf = 100$ and $EO = 300$ case. Modes associated with $m = 0$ and $m \geq 3$ have $\beta_R \leq 0$ for all values of Nf , EO , and U_m studied, and play no role in the transition to linear instability. Furthermore, for all the cases examined, the eigenvalues associated with the $m = 1$ and $m = 2$ modes are real.

From Figure 4, it is seen that for $Nf = 40, 60, 80, 100$, increasing EO is accompanied by a decrease in the magnitude of U_m required for instability and a widening of ΔU_m though this trend appears to saturate at large EO . Moreover, in Figure 5, which depicts the variation of β_R with EO and with $Nf = 80$ held constant, the critical EO for which the $m = 1$ mode is destabilised is reduced threefold as U_m is varied from -0.2 to -0.55 . Thus, the results presented in Figures 4 and 5 demonstrate that increasing the velocity of

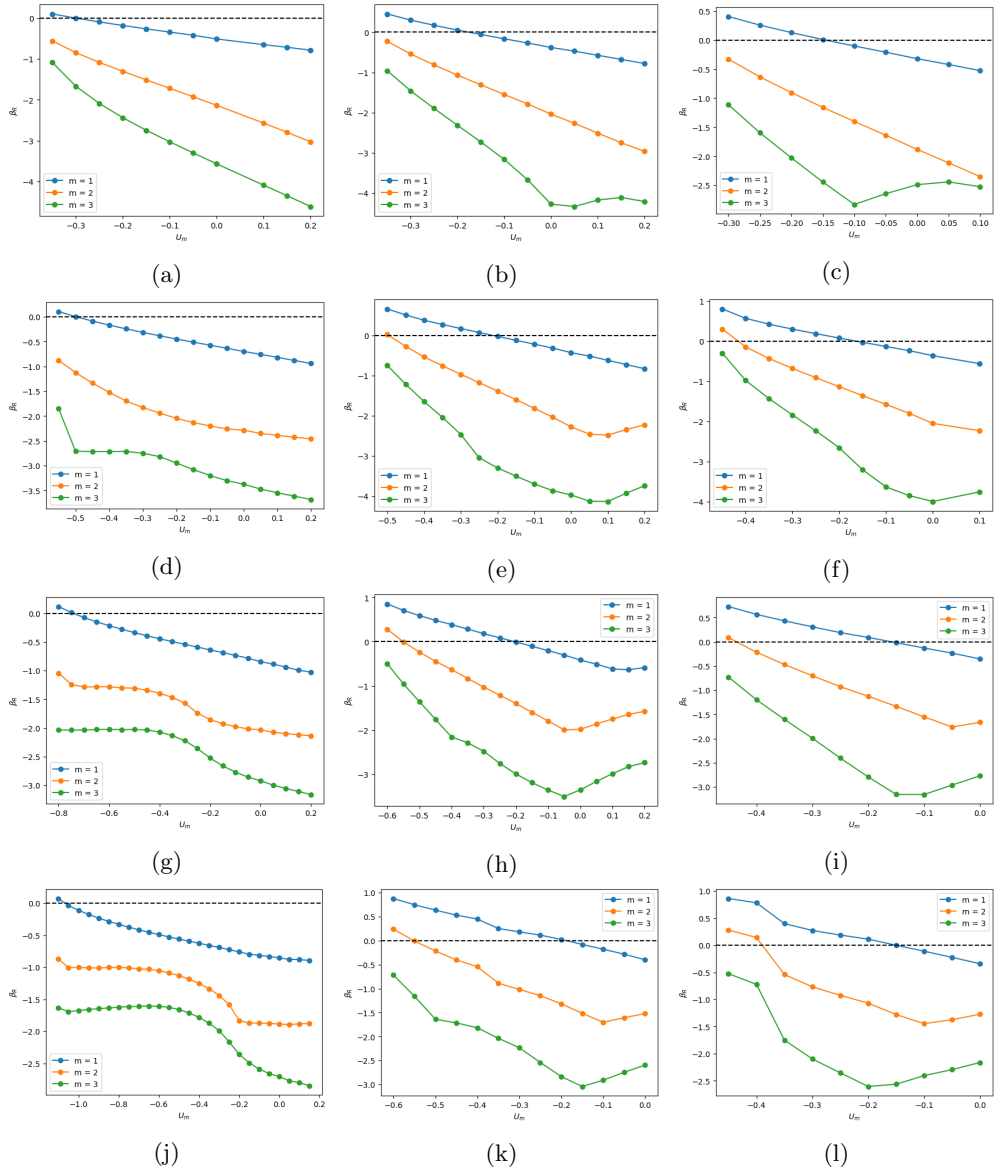


Figure 4: Growth rate, β_R , as a function of U_m for $Nf = 40, 60, 80$, and 100 , shown in (a)-(c), (d)-(f), (g)-(i), and, (j)-(l), respectively, with $Eo = 20$ in (a), (d), (g), and (j), $Eo = 180$ in (b), (e), (h), and (k), and $Eo = 300$ in (c), (f), (i), and (l). The results are shown for the modes $m = 1, 2$, and 3 .

the downward-flowing liquid and/or decreasing the relative significance of surface tension forces is destabilising.

Inspection of Figure 4 also reveals that decreasing Nf for $Eo = 180$ and $Eo = 300$, that is, for weak surface tension, appears to have little effect on the critical U_m , ΔU_m , and the magnitude of β_R for the most dangerous mode, $m = 1$. In contrast, for $Eo = 20$, decreasing Nf leads to a substantial decrease in the critical U_m value and is therefore strongly destabilising indicating that viscous effects gain in significance as the relative

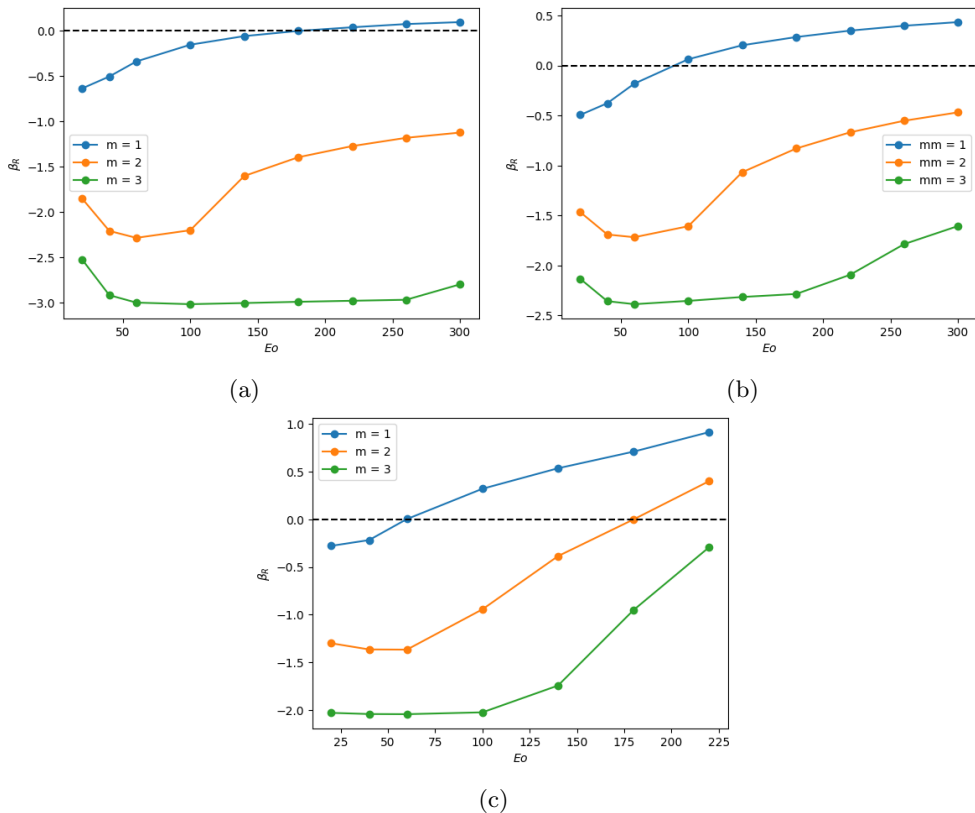


Figure 5: Growth rate, β_R , as a function of Eo , with $Nf = 80$ and $U_m = -0.20$, (a), $U_m = -0.35$, (b) and $U_m = -0.55$, (c). The results are shown for $m = 1, 2$, and 3.

importance of surface tension increases with decreasing Eo for sufficiently low Eo . Furthermore, from Figure 4 (d,a), (e,b) and (f,c), it is also seen that decreasing Nf from $Nf = 60$ to $Nf = 40$ also leads to a large reduction in the critical U_m even at high Eo values for sufficiently small Nf .

We offer an explanation of the trends highlighted above by focusing on the bubble nose and appealing to the steady state results of Abubakar & Matar (2021) who had noted that the frontal radius of curvature of the nose, R_F , in stagnant and downward-flowing liquids increases with Eo then saturates for $Eo \gtrsim 100$ and is weakly-dependent on Nf for $Nf \gtrsim 60$. For $Nf < 60$, R_F is reduced with decreasing Nf . For $Eo < 100$, R_F exhibits a turning point in Eo for all Nf values studied with a well-defined cross-over Eo value below which the magnitude of the R_F minima increase with decreasing Nf . These results demonstrate that bubble noses become flatter with decreasing and increasing Nf for sufficiently small and large Eo , respectively. Abubakar & Matar (2021) have also shown that increasingly negative U_m has a similar effect leading to flatter bubble noses regardless of the value of Nf and Eo ; this is attributed to the increase in the normal stress exerted on the bubble nose relative to that in a stagnant liquid due to the commensurate increase in the opposing inertial force in the downward liquid flow. The results of Abubakar & Matar (2021) for the nose curvature and its dependence on Nf , Eo , and U_m thus appear to mirror the linear stability trends presented in Figures 4-5. In particular, the significant destabilisation of the bubble with Eo increasing from 20

to 180 and its subsequent saturation, the destabilising effect of Nf with decreasing Nf at $EO = 20$ (see figure 4(a,j)), the weak dependence on the stability characteristics for $Nf = 40, 60, 80, 100$ for $EO = 180, 300$ (see Figure 4(b,k) and (c,l)) can be correlated to the parametric dependence of the nose curvature R_F on Nf , EO , and U_m .

3.2. Asymmetric bubble shapes

We now study the influence of the parameters Nf , EO , and U_m on the shapes of the eigenfunctions focusing on those associated with the interfacial deformation in order to highlight the base state bubble regions targeted by the instability. For every point on the three-dimensional axisymmetric base state interface with position vector (r^0, θ^0, z^0) in cylindrical coordinates, from (2.15) and (2.32c), and recalling that $\tilde{\mathbf{x}} = \tilde{h}\mathbf{n}^0$, the corresponding deformed interface points in Cartesian coordinates can be constructed:

$$x = r^0 \cos(\theta^0) + \epsilon [h_R n_r \cos(m\theta^0) - h_I n_r \sin(m\theta^0)] \cos(\theta^0) \quad \forall \theta^0 \in [0, 2\pi] \quad (3.1a)$$

$$y = r^0 \sin(\theta^0) + \epsilon [h_R n_r \cos(m\theta^0) - h_I n_r \sin(m\theta^0)] \sin(\theta^0) \quad \forall \theta^0 \in [0, 2\pi] \quad (3.1b)$$

$$z = z^0 + \epsilon [h_R n_z \cos(m\theta^0) - h_I n_z \sin(m\theta^0)] \quad \forall \theta^0 \in [0, 2\pi] \quad (3.1c)$$

where h_R and h_I denote the real and imaginary parts of the interface deformation in the normal direction; n_r and n_z remain the radial and axial components of the unit normal to the base state interface, respectively. In our discussion below of the three-dimensional bubble shape immediately following the transition to instability, we assign a value to the parameter ϵ , which signifies the formally infinitesimal size of the perturbation, to enhance the visualisation of the results.

Figures 6 and 7 show the influence of the parameters Nf , EO and U_m on the eigenfunctions for the interface deformation \hat{h} . It is seen that the the nose, film, and bottom regions of the bubble are targeted to varying degrees; the precise definitions of these regions are in Abubakar & Matar (2021). For the dominant eigenmode $m = 1$, the peaks in \hat{h} coincide with the nose and bottom regions for high and low EO , respectively. Around the bottom region, the observed peaks in \hat{h} are either due to the tail structure at high EO (see the middle and right column in Figure 6), or the undulation in the film region close to the bubble bottom at low EO (see the left column in Figure 6) though in the latter case we note that the $m = 1$ mode is linearly stable for the parameters used to generate these results ($U_m = -0.2$, $EO = 20$, and $Nf = 40, 60, 80, 100$). For eigenmode $m = 2$, the peak in \hat{h} coincides with the bottom region except at higher magnitude of downward liquid flow velocity, U_m , where similar peaks are seen in the nose region, as shown in Figure 7c. In Figures 6 and 7, we also show enlarged views of the variation of \hat{h} with the arc length s for the bottom region to demonstrate that these boundary layer-like regions in \hat{h} have been resolved adequately.

In Figures 8 and 9, we show the effects of U_m , EO , and Nf on the three-dimensional bubble shapes obtained by adding the interface deformation associated with mode $m = 1$ to the base state taking the value of $\epsilon = 0.05$ for clarity of presentation; these correspond to the shapes one might expect to observe experimentally at the onset of instability. Also shown in Figures 8 and 9 are two-dimensional projections of the shapes in the (r, z) plane which highlight the deviations from the base state within the framework of linear theory. The results shown in Figure 8 are for the same parameter values used to generate Figure 7, which correspond to the large EO , weak surface tension limit; panel (d) of this figure also depicts the analogous results for the deformed bubble shape when $m = 2$. These results illustrate the asymmetry of the nose for Taylor bubble motion in downward flowing liquids for negligible surface tension and are reminiscent of the asymmetric shape shown

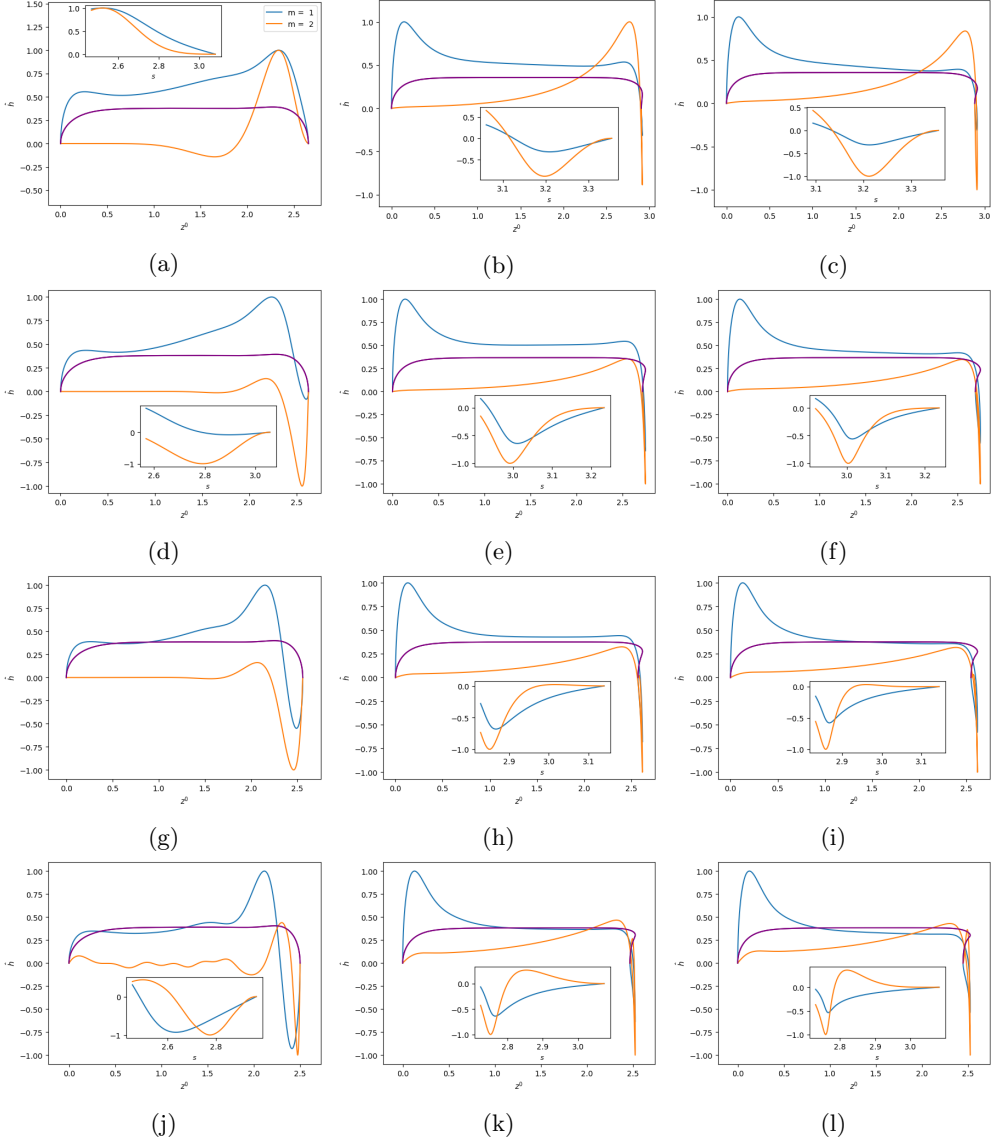


Figure 6: Interface deformation eigenfunctions \hat{h} for eigenmodes $m = 1$ and $m = 2$ as a function of base state axial position of the interface, z^0 , with $U_m = -0.20$ and $Nf = 40, 60, 80,$ and 100 , shown in (a)-(c), (d)-(f), (g)-(i), and (j)-(l), respectively, with $Eo = 20$ in (a), (d), (g), and (j), $Eo = 180$ in (b), (e), (h), and (k), and $Eo = 300$ in (c), (f), (i), and (l). The axisymmetric base state bubble shape is also shown (coloured purple) as a reference in order to highlight the regions targeted by the instability. The insets depict enlarged views of \hat{h} varying with the arc length s for $m = 1$ and $m = 2$ in the bubble bottom region.

in Figure 1b. In Figure 9, on the other hand, the results are associated with $Eo = 20$ at which surface tension effects are significant. Here, it is clearly seen that in addition to asymmetries in the nose region, the instability also targets the undulation in the bottom region. Figure 9d provides a clear demonstration that the asymmetry is most pronounced

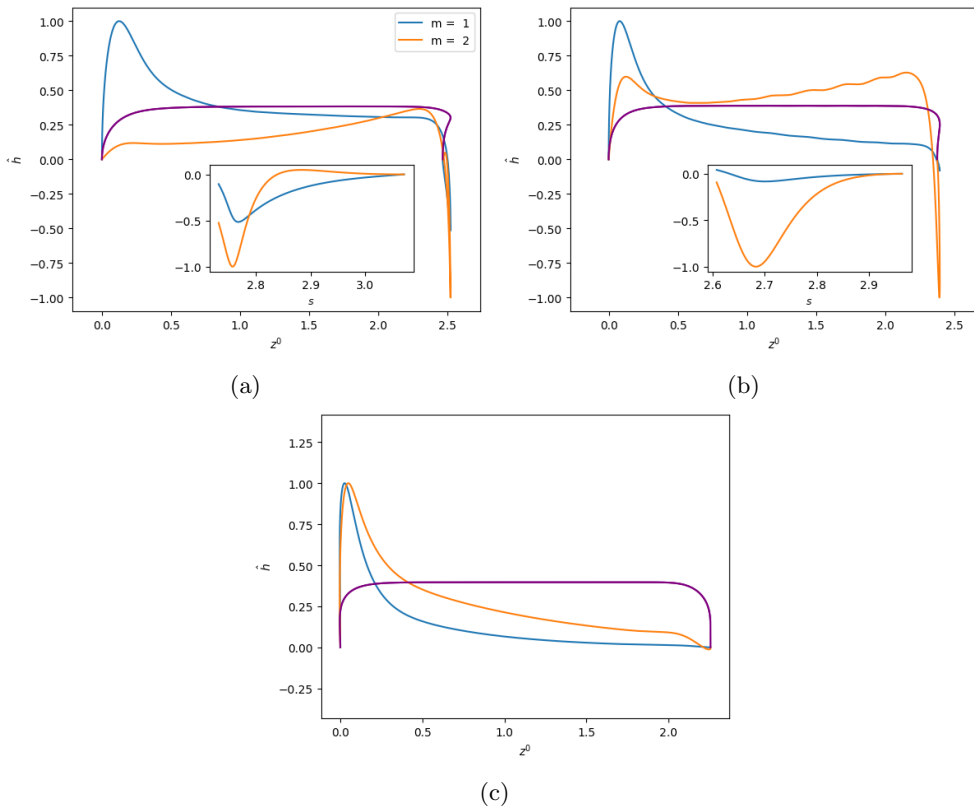


Figure 7: Interface deformation eigenfunctions \hat{h} for eigenmodes $m = 1$ and $m = 2$ as a function of base state axial position of the interface, z^0 , for $Nf = 100$, $EO = 220$, and with $U_m = -0.25$, (a), $U_m = -0.40$, (b), and $U_m = -0.55$, (c). The axisymmetric base state bubble shape is also shown (coloured purple) in order to highlight the regions targeted by the instability. The insets depict enlarged views of \hat{h} varying with the arc length s for $m = 1$ and $m = 2$ in the bubble bottom region.

in this region for the fastest downward flowing liquid case; in contrast, the bubble nose remains essentially axisymmetric in this case.

3.3. Stability maps

We show in Figure 10 stability maps in (U_m, EO) with Nf varying parametrically that depict the boundaries demarcating regions of linear instability for Taylor bubbles moving in downward flowing liquids characterised by $U_m < 0$. In each case, examples of the three-dimensional, asymmetric bubble shape at the onset of instability is also shown. The general trend observed is that for $EO > 60$, the magnitude of the critical U_m decreases with increasing EO for a fixed Nf , saturating for large EO and Nf , beyond $EO \gtrsim 100$ and $Nf \gtrsim 60$. For $EO < 60$, there is a turning point in the stability map that highlights the fact that an increase in the magnitude of the downward flow velocity is needed to overcome the strong surface tension forces at sufficiently low EO ; furthermore, the critical U_m magnitude increases with Nf reflecting the destabilising effect of viscous stresses over this range of EO . The results presented in Figure 10 are consistent with the trends discussed in the previous sections, and, in particular, those associated with the

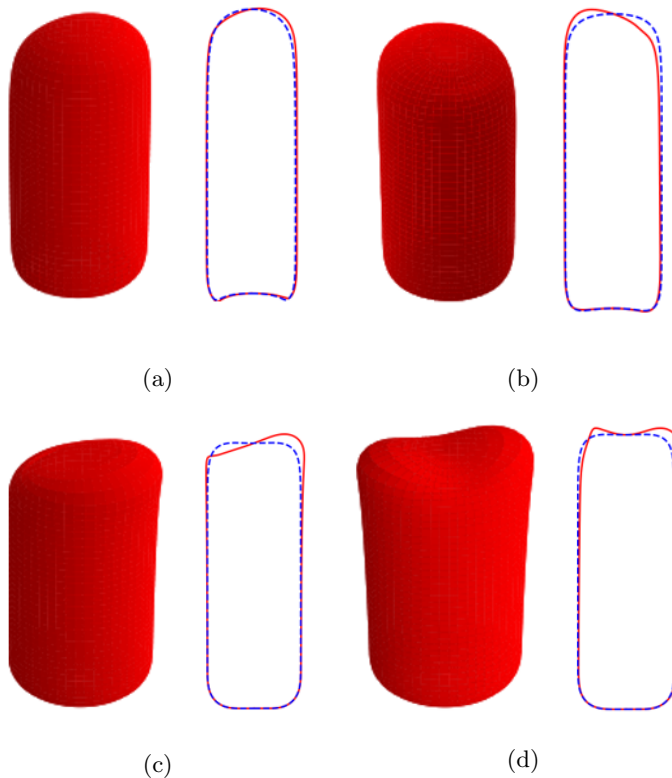


Figure 8: Three-dimensional bubble shapes and their two-dimensional projections (solid lines) in the (r, z) plane obtained by adding the interface deformation for $m = 1$ to the base state (dashed lines) with $\epsilon = 0.05$ for $U_m = -0.25, -0.40, -0.55$, shown in (a)-(c), respectively, with $Nf = 100$ and $EO = 220$. In (d), we show the analogous shape for $m = 2$ with $U_m = -0.55$, $Nf = 100$, and $EO = 220$.

normalised frontal radius of curvature of the nose, R_F , presented in Abubakar & Matar (2021); this provides a further indication that the dependence of R_F on U_m , EO , and Nf controls the linear stability characteristics of the bubble motion.

We also show in Figure 10 the curve for the critical U_m for which the axisymmetric base state has $U_b = 0$. It is noticeable that for $EO \gtrsim 100$ for all Nf studied, this curve is in the linearly unstable region indicating that bubbles whose motion has been arrested due to a downward flowing liquid over this range of EO and Nf cannot have an axisymmetric shape. In contrast, in the complementary range of EO , the critical U_m curve for such bubbles is outside the unstable region implying that they can sustain an axisymmetric shape despite the downward liquid flow. Examples of these cases have been observed experimentally; see, for instance, the axisymmetric Taylor bubble shown to have been held stationary in downward liquid flow by Nigmatulin (2001), for $Nf = 6087.38$ and $EO = 33.06$. We note that the EO value is within the range of the linearly stable region shown in Figure 10(e). Though the experimental Nf value is outside of the range we studied, the fact that the linear stability boundaries appear to saturate at large Nf suggests that our results can still provide a reasonable indication of the behaviour observed experimentally.

4. Energy budget analysis

In this section, we analyse how energy is transferred from the base flow to the perturbations by studying the growth of the perturbation kinetic energy (Hooper & Boyd 1983; Hu & Joseph 1989). By investigating the contribution of the mechanisms of different physical origin that account for energy production, one can identify the dominant ones that drive instability (Boomkamp & Miesen 1996). This analysis has been used to study destabilising mechanisms in parallel two-phase flows (Ó Náraigh *et al.* 2011; Sahu *et al.* 2009, 2007; Selvam *et al.* 2007) and their classification (Boomkamp & Miesen 1996).

4.1. Energy balance formulation

To derive the equation for the growth of the disturbance kinetic energy, one multiplies the continuous forms of the momentum perturbation equations for the velocity components with their corresponding complex conjugates, integrates over the domain, adds the resulting equations, and simplifies as appropriate. Our perturbation equations for the velocity components, however, were derived from the weak form of the continuous momentum equations written around the perturbed domain; the development of the weak form of the energy equation must therefore follow the same strategy. Thus, we obtain the energy equation from the derived perturbation equations for the velocity components by setting the test functions for the latter to equal the complex conjugate of the velocity perturbations, $\bar{\Phi}_r = \hat{u}_r^*$, $\bar{\Phi}_\theta = \hat{u}_\theta^*$, $\bar{\Phi}_z = \hat{u}_z^*$, followed by necessary simplifications:

$$\begin{aligned}
\beta_R \int_{\Omega^0} \left\{ |\hat{u}_r|^2 + |\hat{u}_\theta|^2 + |\hat{u}_z|^2 \right\} d\Omega^0 + \int_{\Omega^0} \left\{ |\hat{u}_r|^2 \frac{\partial u_r^0}{\partial r^0} + |\hat{u}_z|^2 \frac{\partial u_z^0}{\partial z} + \frac{|\hat{u}_\theta|^2 u_r^0}{r} \right. \\
+ \left. \left(\frac{\partial u_r^0}{\partial z} + \frac{\partial u_z^0}{\partial r^0} \right) \Re \{ \hat{u}_r \hat{u}_z^* \} \right\} d\Omega^0 + \int_{\Omega} N f^{-1} \left\{ 2 \left| \frac{\partial \hat{u}_r}{\partial r} \right|^2 + 2 \left| \frac{\partial \hat{u}_z}{\partial z} \right|^2 \right. \\
+ \frac{1}{r^2} \left[(2 + m^2) |\hat{u}_r|^2 + (1 + 2m^2) |\hat{u}_\theta|^2 + m^2 |\hat{u}_z|^2 \right] + \left| \frac{\partial \hat{u}_\theta}{\partial r} \right|^2 + \left| \frac{\partial \hat{u}_\theta}{\partial z} \right|^2 \\
+ \left| \frac{\partial \hat{u}_r}{\partial z} + \frac{\partial \hat{u}_z}{\partial r} \right|^2 - \frac{1}{r} \frac{\partial |\hat{u}_\theta|^2}{\partial r} + \frac{6m}{r^2} \Im m \{ \hat{u}_r \hat{u}_\theta^* \} + \frac{2m}{r} \Im m \left(\hat{u}_z^* \frac{\partial \hat{u}_\theta}{\partial z} + \hat{u}_r^* \frac{\partial \hat{u}_\theta}{\partial r} \right) \left. \right\} d\Omega^0 \\
- \int_{\Gamma_b^0} E o^{-1} \left\{ -\frac{d\hat{h}}{ds} \left[\mathbf{n} \cdot \frac{d\hat{\mathbf{u}}^*}{ds} - \kappa_a (\mathbf{t} \cdot \hat{\mathbf{u}}^*) \right] + \hat{h} \left[\kappa_a^2 + \kappa_b^2 - \frac{m^2}{r^2} \right] \mathbf{n} \cdot \hat{\mathbf{u}}^* \right\} d\Gamma_b^0 \\
- \int_{\Gamma_b^0} \left\{ \hat{h} n_z (\mathbf{n} \cdot \hat{\mathbf{u}}^*) \right\} d\Gamma_b^0 \\
+ \int_{\Gamma_b^0} \hat{h} \left\{ (\mathbf{u}^0 \cdot \mathbf{t}) \left[\frac{d\mathbf{u}^0}{ds} \cdot \hat{\mathbf{u}}^* \right] + \left[-p^0 + 2N f^{-1} \left(\mathbf{t} \cdot \frac{d\mathbf{u}^0}{ds} \right) \right] \left(\mathbf{t} \cdot \frac{d\hat{\mathbf{u}}^*}{ds} \right) \right. \\
+ \left. \left[-p^0 + 2N f^{-1} \frac{u_r^0}{r} \right] \left(\frac{\hat{u}_r^*}{r} - i m \frac{\hat{u}_\theta^*}{r} \right) \right\} d\Gamma_b^0 \\
+ \int_{\Gamma_b^0} \left\{ \left[E o^{-1} \kappa + z - P_b^0 \right] \left[(\mathbf{t} \cdot \hat{\mathbf{u}}^*) \frac{d\hat{h}}{ds} + \hat{h} \left(i m \frac{\hat{u}_\theta^*}{r} \right) + \hat{h} \kappa (\mathbf{n} \cdot \hat{\mathbf{u}}^*) \right] \right\} d\Gamma_b^0 = 0 \quad (4.1)
\end{aligned}$$

where the symbol $|\cdot|$ represents the magnitude of a complex function; \Re and \Im denote the real and imaginary part of a complex function, respectively. Equation (4.1) is the energy budget formulation that governs the evolution of the disturbance kinetic equation.

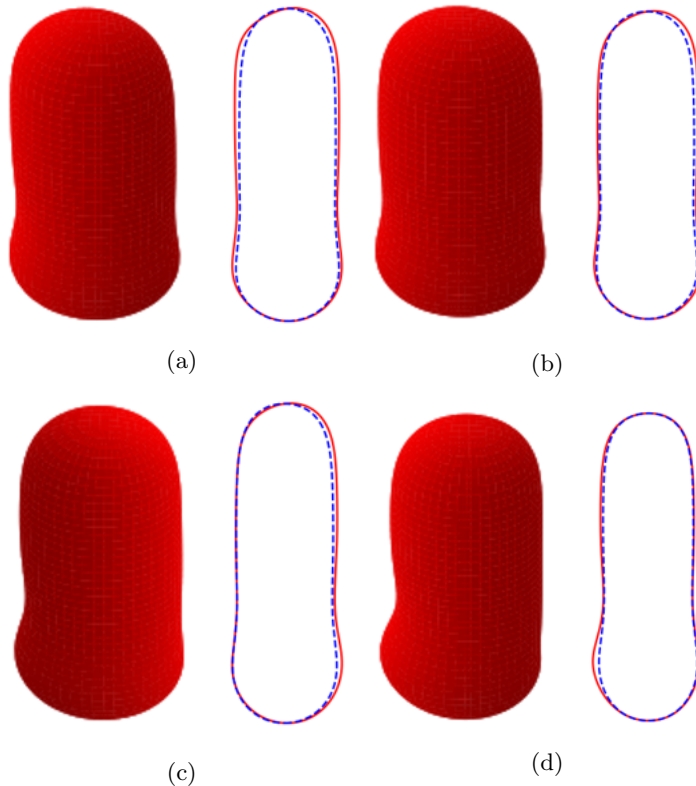


Figure 9: Three-dimensional bubble shapes and their two-dimensional projections (solid lines) in the (r, z) plane obtained by adding the interface deformation for $m = 1$ to the base state (dashed lines) with $\epsilon = 0.05$ for $U_m = -0.35, -0.55, -0.80, -1.10$, and $Nf = 40, 60, 80, 100$, shown in (a)-(d), respectively, with $Eu = 20$.

Following Boomkamp & Miesen (1996), we express the energy balance equation as

$$\dot{E} = REY + DIS + INT, \quad (4.2)$$

where \dot{E} corresponds to the time range of change of the perturbation kinetic energy given by the following relation

$$\dot{E} = \beta_R \int_{\Omega^0} \left\{ |\hat{u}_r|^2 + |\hat{u}_\theta|^2 + |\hat{u}_z|^2 \right\} d\Omega^0 \equiv \beta_R KIN, \quad (4.3)$$

wherein KIN represents the total kinetic energy associated with the perturbation velocity field, which equals \dot{E} when multiplied by the growth rate β_R (which is positive for an unstable flow). We also introduce the following definitions for the terms REY and DIS that appear on the right-hand-side of equation (4.2) (Boomkamp & Miesen 1996):

$$REY = - \int_{\Omega^0} \left\{ |\hat{u}_r|^2 \frac{\partial u_r^0}{\partial r^0} + |\hat{u}_z|^2 \frac{\partial u_z^0}{\partial z} + \frac{|\hat{u}_\theta|^2 u_r^0}{r} + \left(\frac{\partial u_r^0}{\partial z} + \frac{\partial u_z^0}{\partial r^0} \right) \Re \{ \hat{u}_r \hat{u}_z^* \} \right\} d\Omega^0, \quad (4.4)$$

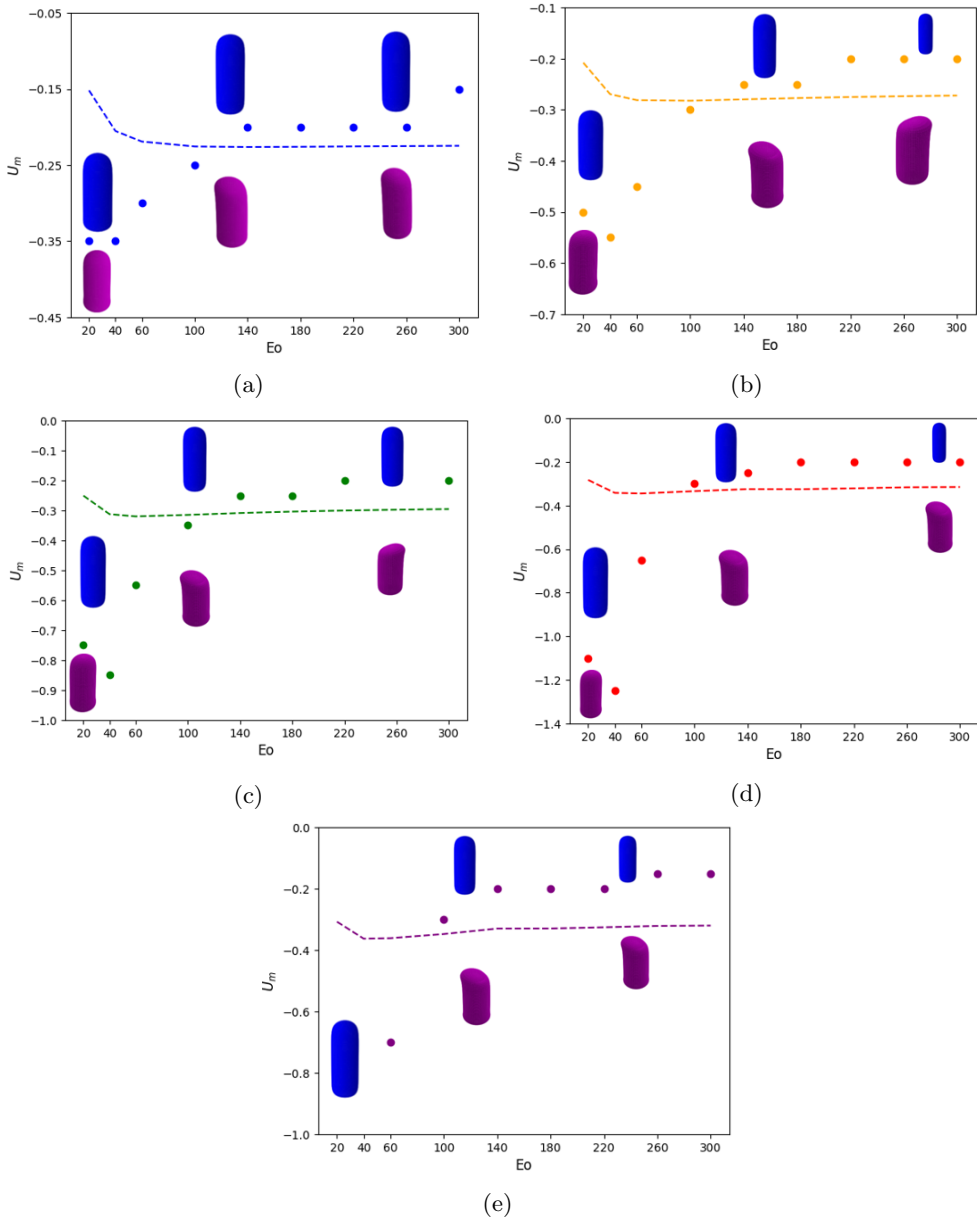


Figure 10: Stability maps depicting the boundaries demarcating (shown by the full circles) the regions of linear instability in (U_m, Eo) space characterised by a transition from axisymmetric to asymmetric bubble shapes in downward liquid flow with $U_m < 0$ for (a) $Nf = 40$, (b) $Nf = 60$, (c) $Nf = 80$, (d) $Nf = 100$ (e) $Nf = 120$. The dashed lines represent the curves of critical U_m for which the axisymmetric base state corresponds to an arrested bubble in downward liquid flow with $U_b = 0$.

$$\begin{aligned}
DIS = & - \int_{\Omega} N f^{-1} \left\{ 2 \left| \frac{\partial \hat{u}_r}{\partial r} \right|^2 + 2 \left| \frac{\partial \hat{u}_z}{\partial z} \right|^2 + \frac{1}{r^2} \left[(2 + m^2) |\hat{u}_r|^2 + (1 + 2m^2) |\hat{u}_\theta|^2 \right. \right. \\
& + m^2 |\hat{u}_z|^2 \left. \right] + \left| \frac{\partial \hat{u}_\theta}{\partial r} \right|^2 + \left| \frac{\partial \hat{u}_\theta}{\partial z} \right|^2 + \left| \frac{\partial \hat{u}_r}{\partial z} + \frac{\partial \hat{u}_z}{\partial r} \right|^2 - \frac{1}{r} \frac{\partial |\hat{u}_\theta|^2}{\partial r} + \frac{6m}{r^2} \Im m \{ \hat{u}_r \hat{u}_\theta^* \} \\
& \left. + \frac{2m}{r} \Im m \left(\hat{u}_z^* \frac{\partial \hat{u}_\theta}{\partial z} + \hat{u}_r^* \frac{\partial \hat{u}_\theta}{\partial r} \right) \right\} d\Omega. \tag{4.5}
\end{aligned}$$

Here, REY denotes the rate of energy transfer by the Reynolds stress from the base flow to the disturbed flow, and DIS represents the rate of viscous dissipation of energy of the disturbed flow. We also provide a breakdown for INT , the rate of work done by the velocity and stress disturbances in deforming the interface (Boomkamp & Miesen 1996)

$$INT = NOR + TAN, \tag{4.6a}$$

$$NOR = TEN + HYD + BUB, \tag{4.6b}$$

which we have decomposed into its normal, NOR , and tangential, TAN , components with NOR further subdivided into TEN , HYD , and BUB , representing work done at the interface against surface tension, gravity, and bubble pressure, respectively. Expressions for TAN , NOR , and TEN , HYD and BUB , are respectively provided by

$$\begin{aligned}
TAN = & \mathbb{R} \left\{ - \int_{\Gamma_b^0} \hat{h} \left\{ (\mathbf{u}^0 \cdot \mathbf{t}) \left[\frac{d\mathbf{u}^0}{ds} \cdot \hat{\mathbf{u}}^* \right] + \left[-p^0 + 2Nf^{-1} \left(\mathbf{t} \cdot \frac{d\mathbf{u}^0}{ds} \right) \right] \left(\mathbf{t} \cdot \frac{d\hat{\mathbf{u}}^*}{ds} \right) \right. \right. \\
& + \left[-p^0 + 2Nf^{-1} \frac{u_r^0}{r} \right] \left(\frac{\hat{u}_r^*}{r} - im \frac{\hat{u}_\theta^*}{r} \right) \left. \right\} d\Gamma_b^0 + \int_{\Gamma_b^0} Eo^{-1} \left\{ \frac{d\hat{h}}{ds} [\kappa_a (\mathbf{t} \cdot \hat{\mathbf{u}}^*)] \right\} d\Gamma_b^0 \\
& - \int_{\Gamma_b^0} \left\{ [Eo^{-1} \kappa + z - P_b^0] \left[(\mathbf{t} \cdot \hat{\mathbf{u}}^*) \frac{d\hat{h}}{ds} + \hat{h} \left(im \frac{\hat{u}_\theta^*}{r} \right) \right] \right\} d\Gamma_b^0, \tag{4.7}
\end{aligned}$$

$$\begin{aligned}
NOR = & \mathbb{R} \left\{ \int_{\Gamma_b^0} Eo^{-1} \left\{ - \frac{d\hat{h}}{ds} \left[\mathbf{n} \cdot \frac{d\hat{\mathbf{u}}^*}{ds} \right] + \hat{h} \left[\kappa_a^2 + \kappa_b^2 - \frac{m^2}{r^2} \right] \mathbf{n} \cdot \hat{\mathbf{u}}^* \right\} d\Gamma_b^0 \right. \\
& \left. + \int_{\Gamma_b^0} \left\{ \hat{h} n_z (\mathbf{n} \cdot \hat{\mathbf{u}}^*) \right\} d\Gamma_b^0 - \int_{\Gamma_b^0} \left\{ [Eo^{-1} \kappa + z - P_b^0] \left[\hat{h} \kappa (\mathbf{n} \cdot \hat{\mathbf{u}}^*) \right] \right\} d\Gamma_b^0 \right\}, \tag{4.8}
\end{aligned}$$

$$TEN = \mathbb{R} \left\{ \int_{\Gamma_b^0} Eo^{-1} \left\{ - \frac{d\hat{h}}{ds} \left[\mathbf{n} \cdot \frac{d\hat{\mathbf{u}}^*}{ds} \right] + \hat{h} \left[\kappa_a^2 + \kappa_b^2 - \kappa^2 - \frac{m^2}{r^2} \right] \mathbf{n} \cdot \hat{\mathbf{u}}^* \right\} d\Gamma_b^0 \right\}, \tag{4.9}$$

$$HYD = \mathbb{R} \left\{ \int_{\Gamma_b^0} \left\{ \hat{h} (n_z - z\kappa) (\mathbf{n} \cdot \hat{\mathbf{u}}^*) \right\} d\Gamma_b^0 \right\}, \tag{4.10}$$

$$BUB = \mathbb{R} \left\{ \int_{\Gamma_b^0} \left\{ P_b^0 \left[\hat{h} \kappa (\mathbf{n} \cdot \hat{\mathbf{u}}^*) \right] \right\} d\Gamma_b^0 \right\}. \tag{4.11}$$

Table 1: Balance of energy distribution among the various energy terms in equation (4.12) for $Nf = 80$, $EO = 140$, and mode $m = 1$.

U_m	β_R	REY^*	DIS^*	TEN^*	HYD^*	BUB^*	TAN^*	SUM	DIF
-0.40	0.2824	-0.0059	-2.6795	-0.1070	0.3066	5.9845	-3.21631	0.2824	2.78×10^{-8}
-0.30	0.1128	0.1224	-2.6494	0.0528	0.5397	3.1162	-1.0690	0.1128	1.85×10^{-7}
-0.20	-0.6354	0.2656	-2.6537	0.2919	0.8280	0.9208	0.2840	-0.6354	$4.2.0 \times 10^{-8}$
-0.10	-0.2442	0.3260	-2.6008	0.5245	1.2070	-0.5126	0.8117	-0.2442	2.23×10^{-6}
0.00	-0.4474	0.2269	-2.1745	0.5412	1.1340	-0.9108	0.7358	-0.4473	1.40×10^{-5}
0.10	-0.6404	0.0413	-1.6299	0.4210	0.6429	-0.5639	0.4481	-0.6404	-7.67×10^{-6}

We normalised the energy terms using KIN , so the energy balance equation becomes

$$\beta_R = REY^* + DIS^* + TEN^* + HYD^* + BUB^* + TAN^*, \quad (4.12)$$

where the asterisk designates the normalisation by KIN . In Table 1, we demonstrate for eigenmode $m = 1$, $Nf = 80$, and $EO = 140$, and various U_m values, that the difference between the growth rate β_R on the left-hand-side of (4.12) computed from the linear stability analysis and the sum of the energy terms on the right-hand-side of (4.12), SUM , denoted as DIF in Table 1 is negligibly small. These results inspire confidence in our procedure for computing the terms in (4.12).

4.2. Energy analysis results

From the linear stability analysis results for downward liquid flow presented in section 3, the $m = 1$ mode was identified as being the most unstable one. Here, we examine the contribution of each term in equation (4.12) in order to elucidate their roles in driving instability and to identify the most dominant destabilising mechanism. In Figure 11, the energy analysis results for $Nf = 80$ with $EO = 20, 180$, and 300 are shown. These parameter values are chosen to correspond to those used to generate a representative subset of the results presented in section 3. In the discussion below, the asterisk decoration which appears in equation (4.12) is suppressed for the sake of brevity.

It is seen clearly in Figure 11a that for $EO = 20$, TAN is overwhelmingly the dominant mechanism, followed by BUB , over the range of U_m for which $\beta_R > 0$. Over the remainder of the U_m range studied in which $\beta_R < 0$, TAN decreases monotonically but remains destabilising while BUB becomes stabilising. HYD , REY , and TEN are destabilising over this range while, as expected, DIS is stabilising. Upon increasing EO to 180 and 300 , as shown in Figure 11b and 11c, respectively, the dominant mechanism over the unstable range of U_m switches to BUB followed in relative dominance by HYD , which is marginally destabilising, while TAN is strongly stabilising. These results suggest that the dominant mechanism depends on the relative significance of surface tension forces. In the case of negligible surface tension, characterised by high EO values, the destabilising mechanism is related to the bubble pressure which indicates that the origin of the instability is in the gas phase. At low EO , the instability originates in the liquid phase with the energy provided by the tangential stress component.

It is instructive to split TAN , given by equation (4.7), into its constituent components

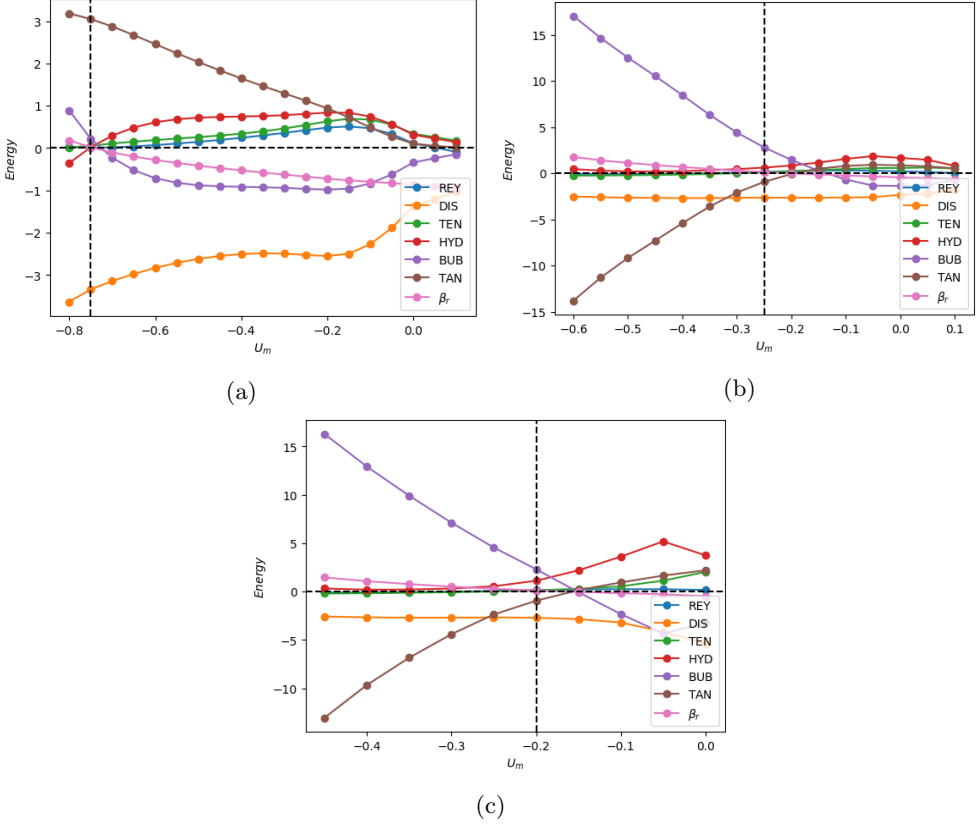


Figure 11: Breakdown of the energy budget for the eigenmode $m = 1$ as a function of U_m for $Eo = 20, 180$, and 300 , shown in (a)-(c), respectively, with $Nf = 80$. In each panel, the vertical dashed line marks the U_m value for which $\beta_R = 0$.

based on the base state groups that supply energy to the perturbations:

$$TAN_{ut} = \mathbb{R} \left\{ - \int_{\Gamma_b^0} \hat{h}(\mathbf{u}^0 \cdot \mathbf{t}) \left[\frac{d\mathbf{u}^0}{ds} \cdot \hat{\mathbf{u}}^* \right] \right\}, \quad (4.13a)$$

$$TAN_{strs} = \mathbb{R} \left\{ - \int_{\Gamma_b^0} \hat{h} \left\{ \left[-p^0 + 2Nf^{-1} \left(\mathbf{t} \cdot \frac{d\mathbf{u}^0}{ds} \right) \right] \left(\mathbf{t} \cdot \frac{d\hat{\mathbf{u}}^*}{ds} \right) + \left[-p^0 + 2Nf^{-1} \frac{u_r^0}{r} \right] \left(\frac{\hat{u}_r^*}{r} - im \frac{\hat{u}_\theta^*}{r} \right) \right\} \right\}, \quad (4.13b)$$

$$TAN_{ts} = \mathbb{R} \left\{ \int_{\Gamma_b^0} Eo^{-1} \left\{ \frac{d\hat{h}}{ds} [\kappa_a (\mathbf{t} \cdot \hat{\mathbf{u}}^*)] - \kappa \left[(\mathbf{t} \cdot \hat{\mathbf{u}}^*) \frac{d\hat{h}}{ds} + \hat{h} \left(im \frac{\hat{u}_\theta^*}{r} \right) \right] \right\} d\Gamma_b^0 \right\}, \quad (4.13c)$$

$$TAN_g = \mathbb{R} \left\{ \int_{\Gamma_b^0} -z \left[(\mathbf{t} \cdot \hat{\mathbf{u}}^*) \frac{d\hat{h}}{ds} + \hat{h} \left(im \frac{\hat{u}_\theta^*}{r} \right) \right] d\Gamma_b^0 \right\}, \quad (4.13d)$$

$$TAN_{pb} = \mathbb{R} \left\{ \int_{\Gamma_b^0} P_b \left[(\mathbf{t} \cdot \hat{\mathbf{u}}^*) \frac{d\hat{h}}{ds} + \hat{h} \left(im \frac{\hat{u}_\theta^*}{r} \right) \right] d\Gamma_b^0 \right\}. \quad (4.13e)$$

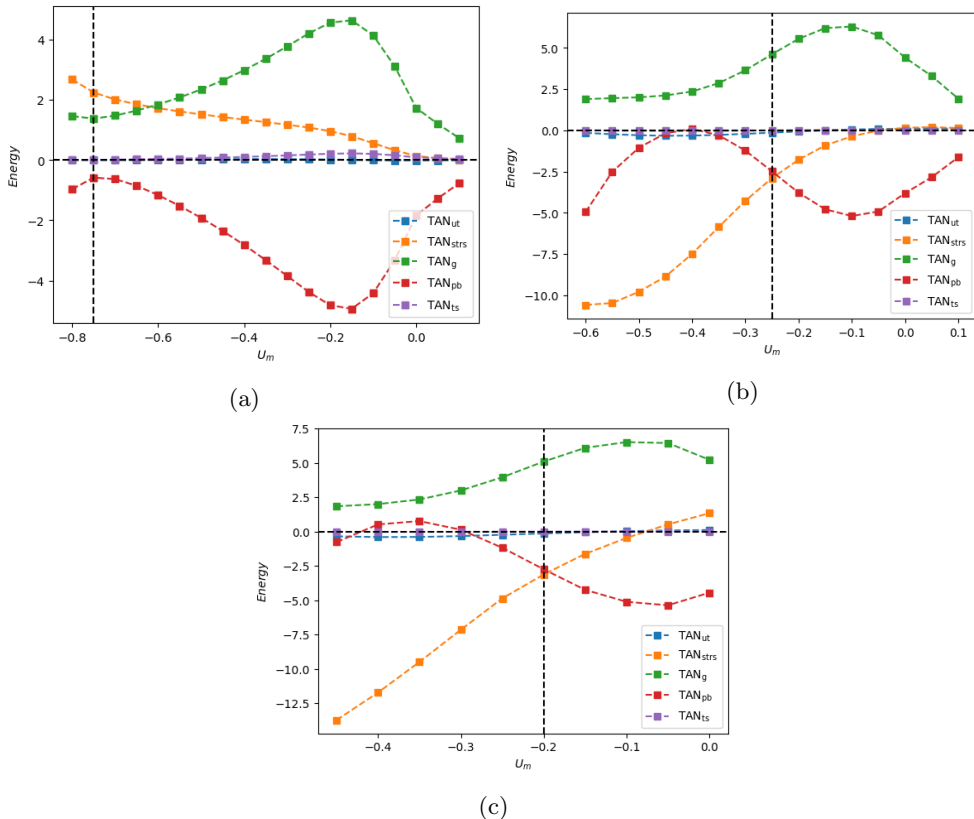


Figure 12: Breakdown of TAN for the eigenmode $m = 1$ into its constituent components given by equations (4.13) as a function of U_m for $Eo = 20, 180$, and 300 , shown in (a)-(c), respectively, with $Nf = 80$. In each panel, the vertical dashed line marks the U_m value for which $\beta_R = 0$.

The terms TAN_{ut} , TAN_{strs} , TAN_{ts} , TAN_g and TAN_{pb} denote the contributions to TAN due to streaming tangential velocity, tangential stress, surface tension, gravity and bubble pressure on the interface as captured by the base state terms $\mathbf{u} \cdot \mathbf{t}$, $\left[-p^0 + 2Nf^{-1} \left(\mathbf{t} \cdot \frac{d\mathbf{u}^0}{ds}\right)\right] + \left[-p^0 + 2Nf^{-1} \frac{u_r^0}{r}\right]$, Eo , z and P_b in the expressions, respectively. The base state contribution to TAN_{strs} is related to the tangential stress because it can be obtained by taking the double dot product of the stress tensor and the tangential projection operator, $(\mathbf{I} - \mathbf{n} \otimes \mathbf{n})$.

In Figure 12, we plot the dependence of the constituents of TAN on U_m for $m = 1$, $Eo = 20, 180$, and 300 , and $Nf = 80$. Inspection of Figure 12(a) reveals that in the $Eo = 20$ case, for which surface tension effects are important, the major contributor to TAN corresponds to TAN_{strs} and exerts a destabilising influence on the bubble motion. As can also be seen in Figure 12a, although TAN_{strs} remains destabilising, it gives way to TAN_g as the dominant contributor to TAN with decreasing magnitude of U_m , while TAN_{pb} is sufficiently stabilising so as to render $\beta_R < 0$; the contributions of TAN_{ut} and TAN_{ts} are relatively negligible and they play an insignificant role in the bubble stability.

In Figure 12(b,c) generated for $Eo = 180$ and 300 for which surface tension effects are weak, the dominant destabilising contribution to TAN is due to TAN_g with the

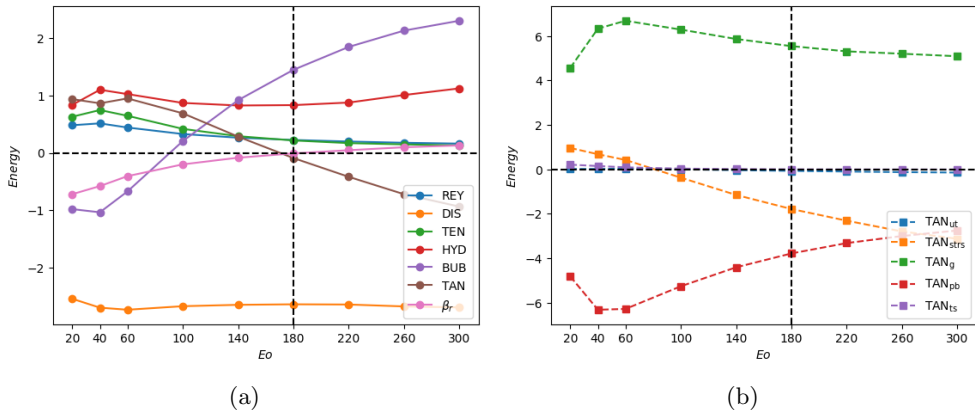


Figure 13: Breakdown of the energy budget (see equation (4.12)), (a), and the TAN constituents (see equation (4.13)), (b), with Eo , for $m = 1$ with $Nf = 80$ and $U_m = -0.20$. The vertical dashed line marks the Eo value for which $\beta_R = 0$.

sub-dominant TAN_{strs} and TAN_{pb} exerting a stabilising influence over the majority of the U_m range investigated. The reversal in the role of TAN_{strs} as we cross over from relatively low to high Eo values shown in Figure 12(b,c) is consistent with the results discussed in the previous sections which indicated that viscous effects are destabilising (stabilising) for low (high) Eo . This is further illustrated in Figure 13 in which we plot the breakdown of the energy budget (see Figure 13a) and the constituents of TAN (see Figure 13b) as a function of Eo for $m = 1$ with $U_m = -0.2$ and $Nf = 80$. It is clear that TAN_{strs} switches roles in the Eo interval (60, 100] and TAN exhibits a similar behaviour over a somewhat larger Eo range.

Lastly, we show in Figure 14a breakdown of the energy budget and of the TAN constituents as a function of Nf for $m = 1$ with $Eo = 300$ and $U_m = -0.25$. It is seen clearly in Figure 14a that for this large Eo case, BUB provides the dominant destabilising contribution with TAN and DIS inducing stability. Inspection of Figure 14b reveals that although TAN_g is destabilising over the range of Nf studied, TAN_{pb} is also destabilising for $Nf < 60$; this acts to reduce the stabilising effect associated with the increase in viscous effects and reduction in Nf .

We now establish a connection with the work of Lu & Prosperetti (2006) who concluded that it is the normal component of gravity on the interface that drives the transition to asymmetric Taylor bubble shape. It is worth mentioning, however, that the analysis of Lu & Prosperetti (2006) was carried out locally around the nose region under the assumptions that the effects of viscosity and surface tension are negligible. In contrast, our analysis shows that the dominant destabilising mechanisms depend on the relative significance of surface tension characterised by Eo : for low and high Eo , the tangential stress, TAN (with TAN_{strs} being the main contributor) and the work done at the interface against the bubble pressure, BUB , are chiefly responsible for instability, respectively. A look at Figures 13a and 14a shows that the energy term due to normal component of gravity on the interface, HYD , is an increasing function of Nf and Eo . It is plausible that at very high Nf and Eo HYD may overtake BUB as the most dominant destabilising energy term. It is therefore likely that the mechanisms governing the instability in regimes of extremely negligible surface tension and viscosity is different from that identified in this investigation.

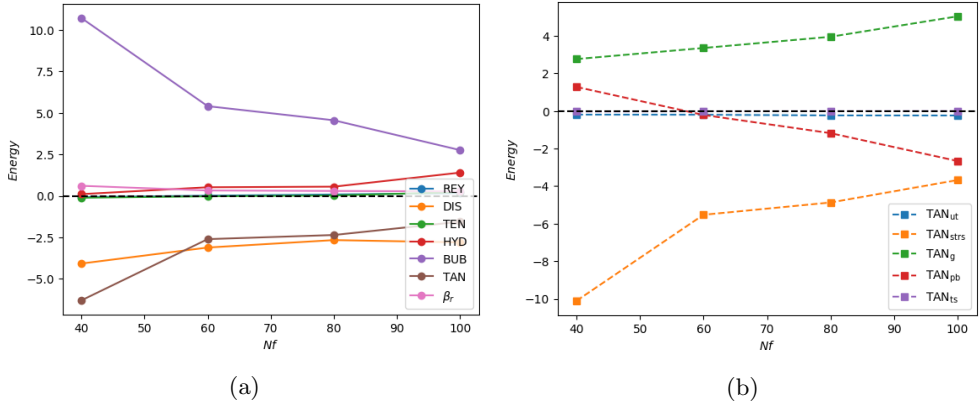


Figure 14: Breakdown of the energy budget (see equation (4.12)), (a), and the TAN constituents (see equation (4.13)), (b), with Nf , for $m = 1$ with $Eo = 300$ and $U_m = -0.25$.

5. Summary and conclusions

We have examined the linear stability of Taylor bubbles in stagnant and flowing liquids in vertical pipes focusing on the case of downward liquid flow. The base state, characterised by constant bubble and axisymmetric shapes, was computed by Abubakar & Matar (2021) as a function of the Eötvös and inverse viscosity numbers, Eo and Nf , and the (centreline) speed of the downward flowing liquid, U_m . A finite element linear stability model was derived using the concepts of domain perturbation and total linearisation method presented in Carvalho & Scriven (1999) and Kruyt *et al.* (1988), respectively. The model was validated by comparing its predictions with analytical results for the growth rate and frequency for the normal mode small-amplitude oscillation of a spherical bubble in an unbounded stagnant liquid under the assumption of negligible gravity.

Our linear stability framework was then used to examine the stability of the base states obtained by Abubakar & Matar (2021). Our results demonstrated that the leading unstable mode corresponds to $m = 1$, where m is the azimuthal wavenumber of the applied perturbation. We constructed stability maps showing the dependence of the critical magnitude of U_m on Eo , with Nf varying parametrically, which demarcate the regions in (U_m, Eo) space wherein the flow is linearly unstable. At low Eo , for which surface tension effects are significant, the instability targets an undulation in the bottom region of the bubble with the three-dimensional bubble shape exhibiting an asymmetric bulge in that region. For weak surface tension effects, characterised by high Eo , the most unstable mode corresponds to a deflection of the bubble nose away from the axis of symmetry. The stability maps also show the locus of points for which the bubble are stationary in a downward flowing liquid and highlights the regions in parameter space in which they are linearly stable or unstable resulting in axisymmetric and asymmetric shapes, respectively.

To elucidate the origins of the transition to linear instability and asymmetric bubble shapes, an energy budget analysis was performed to analyse the contribution of various physical mechanisms to the production of perturbation energy. This analysis showed that the major contribution to energy production that drives the instability comes from the bubble pressure and the tangential stress for high and low Eo values, respectively. The insights gained from the energy analysis, and the trends observed in the linear

stability characteristics, were used to establish clear connections to the influence of Eo , Nf , and U_m on the curvature of the bubble nose, which plays a crucial role in the stability of the flow.

Declaration of Interests. The authors report no conflict of interest.

Acknowledgements

This work was supported by the Engineering & Physical Sciences Research Council UK through the EPSRC MEMPHIS (grant no. EP/K003976/1) and PREMIERE (grant no. EP/T000414/1) Programme Grants, and a Nigerian government PTDF scholarship for HA. OKM also acknowledges funding from PETRONAS and the Royal Academy of Engineering for a Research Chair in Multiphase Fluid Dynamics, and the PETRONAS Centre for Engineering of Multiphase Systems. We also acknowledge HPC facilities provided by the Research Computing Service (RCS) of Imperial College London for the computing time.

Appendix A. Weak formulations

The transformation of the governing equations into their weak forms involves three steps: multiplying the governing equations for each variables with their corresponding *test functions* and integrating over the domain, integrating by part to reduce the order of integration, and, finally, incorporating the boundary conditions into the resulting relations. Before proceeding to derive the weak forms of the equations, it is important to define the necessary functional spaces to which the solution and test functions must belong (Heinrich & Pepper 1999):

(i) The $L^2(\Omega)$ space: This is a space of functions $f(\mathbf{r})$ defined in Ω that are square integrable over Ω :

$$L^2(\Omega) = \left\{ f(\mathbf{r}) \mid \int_{\Omega} (f(\mathbf{r}))^2 d\Omega < \infty \right\}. \quad (\text{A } 1)$$

(ii) The $L_0^2(\Omega)$ subspace: This is a subspace of $L^2(\Omega)$ defined in Ω such that for functions defined in $L^2(\Omega)$, the following equation is satisfied:

$$L_0^2(\Omega) = \left\{ f \mid f \in L^2(\Omega) \text{ and } \int_{\Omega} f(\mathbf{r}) = 0 \right\}. \quad (\text{A } 2)$$

(iii) The Sobolev space $H^1(\Omega)$: this is a space of functions $f(\mathbf{r})$ defined in Ω such that both the function and all its first partial derivatives are in $L^2(\Omega)$

$$H^1(\Omega) = \left\{ f(\mathbf{r}) \mid \int_{\Omega} [|f|^2 + |\nabla f|^2] d\Omega < \infty \right\}. \quad (\text{A } 3)$$

(iv) The Sobolev subspace $H_0^1(\Omega)$: this is a subspace of the Sobolev space $H^1(\Omega)$ for which the functions defined in space H^1 vanish on the portions of the boundary of Ω where *Dirichlet* boundary conditions are imposed (i.e $\Gamma_D = \Gamma_{in} + \Gamma_{wall}$):

$$H_0^1(\Omega) = \{ f \mid f \in H^1(\Omega) \text{ and } f(\mathbf{r}) = \mathbf{0} \text{ if } \mathbf{r} \in \Gamma_D \}. \quad (\text{A } 4)$$

Let $\Phi \in H_0^1$ and $\varphi \in L_0^2$ be the test functions corresponding to $\mathbf{u} \in H^1$ and $\mathbf{p} \in L^2$, respectively. Next we take the inner product of equation (2.1) with Φ , multiply equation

(2.2) with φ and integrate the equations over the domain:

$$\int_{\Omega} \left\{ \frac{\partial \mathbf{u}}{\partial t} \cdot \Phi + [(\mathbf{u} \cdot \nabla) \mathbf{u}] \cdot \Phi - [\nabla \cdot \mathbf{T}] \cdot \Phi \right\} d\Omega = 0, \quad (\text{A } 5)$$

$$\int_{\Omega} \{(\nabla \cdot \mathbf{u}) \varphi\} d\Omega = 0. \quad (\text{A } 6)$$

Equations (A 5) and (A 6) are the weighted residual forms of the momentum and continuity equations, respectively. Integrating the last term on the left-hand-side of (A 5) by parts,

$$\int_{\Omega} \{[\nabla \cdot \mathbf{T}] \cdot \Phi\} d\Omega = \int_{\Gamma} \{\mathbf{n} \cdot \mathbf{T} \cdot \Phi\} d\Gamma_b - \int_{\Omega} \{\mathbf{T} : \nabla(\mathbf{u})\} d\Omega, \quad (\text{A } 7)$$

where

$$\Gamma = \Gamma_b + \Gamma_{in} + \Gamma_{wall} + \Gamma_{out}.$$

Enforcing the outlet boundary condition and taking into consideration that $\Phi \in H_0^1$, hence Φ are zero where *essential* boundary conditions are imposed, we are left with

$$\Gamma = \Gamma_b.$$

Making use of (2.3), equation (A 5) becomes

$$\int_{\Omega} \left\{ \frac{\partial \mathbf{u}}{\partial t} \cdot \Phi + [(\mathbf{u} \cdot \nabla) \mathbf{u}] \cdot \Phi + 2Nf^{-1} \mathbf{E}(\mathbf{u}) : \mathbf{E}(\Phi) - p(\nabla \cdot \Phi) \right\} d\Omega - \int_{\Gamma_b} \{\mathbf{n} \cdot \mathbf{T} \cdot \Phi\} d\Gamma_b = 0. \quad (\text{A } 8)$$

The traction term in the last term on the left-hand-side of (A 8) can be decomposed into its normal and tangential components (Pozrikidis 2011):

$$\mathbf{n} \cdot \mathbf{T} = [\mathbf{n} \cdot \mathbf{T} \cdot \mathbf{n}] \mathbf{n} + \mathbf{n} \times [\mathbf{n} \cdot \mathbf{T} \times \mathbf{n}], \quad (\text{A } 9)$$

thereby allowing the incorporation of normal stress condition (2.8) and tangential stress condition (2.9) into (A 8) to give

$$\int_{\Omega} \left\{ \frac{\partial \mathbf{u}}{\partial t} \cdot \Phi + [(\mathbf{u} \cdot \nabla) \mathbf{u}] \cdot \Phi + 2Nf^{-1} \mathbf{E}(\mathbf{u}) : \mathbf{E}(\Phi) - p(\nabla \cdot \Phi) \right\} d\Omega - \int_{\Gamma_b} \{[Eo^{-1}\kappa + z - P_b] \mathbf{n} \cdot \Phi\} d\Gamma_b = 0. \quad (\text{A } 10)$$

Equations (A 6) and (A 10) are the weak forms of the governing equations.

Appendix B. Curvature linearisation

For a three-dimensional axisymmetric surface, the interface location in any (r, z) plane is sufficient for computing the curvature of the surface. Consider that the interface in any such plane is spanned by a curve with the coordinates of any point on the curve being (r, z) . In addition, let the interface be parametrised by length of arc s so that the

position vector of any point on the interface is given as

$$\mathbf{r} = r(s)\mathbf{i}_r + z(s)\mathbf{i}_z. \quad (\text{B1})$$

The total curvature at any given point on the interface is defined as

$$\kappa = -\nabla_s \cdot \mathbf{n}, \quad (\text{B2})$$

where $r(s)$ and $z(s)$ are the radial and axial coordinates of the points on the interface, respectively; \mathbf{n} remains the unit normal to the interface and ∇_s is the surface tangential gradient operator which is given as

$$\nabla_s = (\mathbf{I} - \mathbf{n} \otimes \mathbf{n}) \nabla. \quad (\text{B3})$$

For a three-dimensional axisymmetric surface, (B3) simplifies to

$$\nabla_s = t_r \frac{d}{ds} \mathbf{i}_r + \frac{1}{r} \frac{\partial}{\partial \theta} \mathbf{i}_\theta + t_z \frac{d}{ds} \mathbf{i}_z, \quad (\text{B4})$$

and equation (B2) becomes

$$\kappa = - \left(\mathbf{t} \cdot \frac{d\mathbf{n}}{ds} + \frac{n_r}{r} \right), \quad (\text{B5})$$

where \mathbf{t} is the unit tangent vector to the interface with components t_r , t_θ and t_z in the radial, azimuthal and axial directions, respectively; $\frac{d}{ds} = (\mathbf{t} \cdot \nabla)$ is an operator that denotes the derivative in the tangential direction; n_r is the radial component of the unit normal vector, \mathbf{n} .

Let us imagine that the deformed interface can be expressed as a summation of the undeformed interface and a very small deformation. Thus, the deformed interface can be written as

$$\mathbf{r} = \mathbf{r}^0 + \mathbf{x}, \quad (\text{B6})$$

where $\mathbf{r}^0 = r^0 \mathbf{i}_r + \theta^0 \mathbf{i}_\theta + z^0 \mathbf{i}_z$ and $\mathbf{r} = r \mathbf{i}_r + \theta \mathbf{i}_\theta + z \mathbf{i}_z$ are the undeformed (i.e base) and deformed (i.e perturbed) interface position vectors, respectively; $\mathbf{x} = x_r \mathbf{i}_r + x_\theta \mathbf{i}_\theta + x_z \mathbf{i}_z$, as mentioned in the previous section, is the interface deformation vector and is taken to be very small in magnitude. Linearisation of the unit normal to, and elemental arc length on, the deformed interface about the undeformed interface give (Kruyt *et al.* 1988; Ramanan & Engelman 1996; Weatherburn 1927)

$$\mathbf{n} = \mathbf{n}^0 - \mathbf{n}^0 \times \nabla_s \times \mathbf{x}, \quad (\text{B7})$$

$$ds = \left(1 + \mathbf{t}^0 \cdot \frac{d\mathbf{x}}{ds^0} \right) ds^0, \quad (\text{B8})$$

$$\frac{d}{ds} = \left(1 - \mathbf{t}^0 \cdot \frac{d\mathbf{x}}{ds^0} \right) \frac{d}{ds^0}. \quad (\text{B9})$$

On further simplification of (B7)

$$\mathbf{n} = \mathbf{n}^0 - \mathbf{t}^0 \left(\mathbf{n}^0 \cdot \frac{d\mathbf{x}}{ds^0} \right) - \frac{\mathbf{n}^0}{r^0} \cdot \frac{\partial \mathbf{x}}{\partial \theta^0} \mathbf{i}_\theta. \quad (\text{B10})$$

Substituting (2.19) together with (B6) and (B9) into (B5), the linearised curvature

neglecting all terms of nonlinear in x gives

$$\kappa = \kappa^0 + \kappa^1, \quad (\text{B 11})$$

with

$$\kappa^0 = - \left(\mathbf{t}^0 \cdot \frac{d\mathbf{n}^0}{ds^0} + \frac{n_r^0}{r^0} \right), \quad (\text{B 12})$$

$$\begin{aligned} \kappa^1 = \frac{1}{r^0} \frac{d}{ds^0} \left[r^0 \left(\mathbf{n}^0 \cdot \frac{d\mathbf{x}}{ds^0} \right) \right] + 2 \left(\mathbf{t}^0 \cdot \frac{d\mathbf{x}}{ds^0} \right) \left(\mathbf{t}^0 \cdot \frac{d\mathbf{n}^0}{ds^0} \right) + \frac{\mathbf{n}^0}{r^{0^2}} \cdot \frac{\partial^2 \mathbf{x}}{\partial \theta^{0^2}} + \frac{x_r n_r^0}{r^{0^2}} \\ - \frac{dn^0}{ds^0} \cdot \frac{d\mathbf{x}}{ds^0}. \end{aligned} \quad (\text{B 13})$$

When (2.20) is further simplified by allowing the deformation vector to be of the form

$$\mathbf{x} = h\mathbf{n}^0, \quad (\text{B 14})$$

it results in

$$\kappa^1 = \frac{1}{r^0} \frac{d}{ds^0} \left(r^0 \frac{dh}{ds^0} \right) + h \left[\kappa_a^{0^2} + \kappa_b^{0^2} + \frac{1}{r^{0^2}} \frac{\partial^2 h}{\partial \theta^{0^2}} \right], \quad (\text{B 15})$$

which is the same as the expression derived for curvature perturbation in Chireux *et al.* (2015), albeit through a different and longer route. In arriving at (B 15), we have used the following Frenet-Serret relations

$$\frac{d\mathbf{t}}{ds} = \kappa\mathbf{n}, \quad (\text{B 16a})$$

$$\frac{d\mathbf{n}}{ds} = -\kappa\mathbf{t}. \quad (\text{B 16b})$$

Equations (B 13) and (B 15) are the expressions for curvature deformation and can be used for an axisymmetric deformation by setting the term containing derivative with respect to the azimuthal coordinate to zero to obtain

$$\kappa^1 = \frac{1}{r^0} \frac{d}{ds^0} \left(r^0 \frac{dh}{ds^0} \right) + h \left[\kappa_a^{0^2} + \kappa_b^{0^2} \right]. \quad (\text{B 17})$$

In equations (B 7)-(B 15), \mathbf{n}^0 is the unit normal vector to the undeformed interface and n_r^0 , n_θ^0 and n_z^0 are its component in the radial, azimuthal and axial directions, respectively; \mathbf{t}^0 is the unit tangent vector to the undeformed interface with components t_r^0 , t_θ^0 and t_z^0 in the radial, azimuthal and axial directions, respectively; ds and ds^0 are the elemental arc length for the deformed and undeformed interfaces, respectively; κ^0 is the curvature of the undeformed surface and κ^1 is the addition to the undeformed interface curvature (also referred to as curvature perturbation in the context of linear stability analysis) due to linearisation of the deformed interface about the undeformed interface; h is the magnitude of the interface deformation in the direction normal to the undeformed interface. κ_a^0 and κ_b^0 are the two principal curvatures of the undeformed interface (B 12) corresponding to

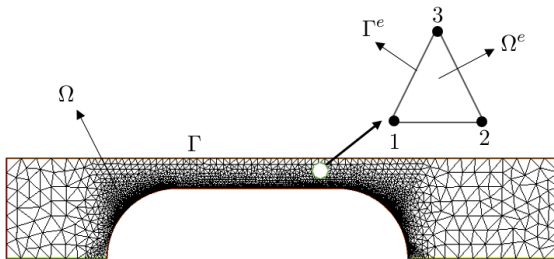


Figure 15: Two-dimensional triangulated domain with linear approximations on the subdomains thereby leading to three nodes.

the curvature in the $r - z$ and $r - \theta$ planes, respectively, defined as

$$\kappa_a^0 = \mathbf{t}^0 \cdot \frac{d\mathbf{n}^0}{ds^0}, \quad (\text{B } 18a)$$

$$\kappa_b^0 = \frac{n_r^0}{r^0}. \quad (\text{B } 18b)$$

Appendix C. Galerkin finite element approximation

In appendix A, we derived the weak forms of the governing equations in the continuous domain. Let us divide the domain, Ω into smaller subsets, *finite element*, so that each element occupies a sub-domain Ω^e with boundary Γ^e . The discretised domain is therefore an assemblage of n_e finite elements that make up the domain:

$$\int_{\Omega^h} \{\cdot\} d\Omega^h = \sum_{k=1}^{n_e} \int_{\Omega_k^e} \{\cdot\} d\Omega_k^e, \quad (\text{C } 1)$$

$$\int_{\Gamma^h} \{\cdot\} d\Gamma^h = \sum_{k=1}^{n_e} \int_{\Gamma_k^e} \{\cdot\} d\Gamma_k^e, \quad (\text{C } 2)$$

where Ω^h represents the discretised domain with boundary Γ^h , and n_e is the number of elements in the discretised domain. The geometry of the finite element could be a triangle or quadrilateral in a two-dimensional domain and in three-dimensional domain, it could be a tetrahedral or hexahedral. On each element, the unknown variables of the problem, known as *trial functions*, are approximated as a linear combination of unknown parameters and piecewise polynomial functions, *basis* (or *shape*) *functions*. In addition, the test functions corresponding to each variables are set to equal to the basis functions used in approximating the variables. Depending on the geometry of an element and the order of polynomial used in approximating the unknown variable on the element, n_v number of nodes/unknown parameters can be associated with the element as shown in

Figure 15. Thus, on each element, the trial and test functions are approximated as

$$\mathbf{u}_r(\mathbf{x}, t) = \sum_{k=1}^{n_v} \psi^k(\mathbf{x}) v_r^k(t) = \Psi^T \mathbf{v}_r, \quad (\text{C } 3a)$$

$$\mathbf{u}_\theta(\mathbf{x}, t) = \sum_{k=1}^{n_v} \psi^k(\mathbf{x}) v_\theta^k(t) = \Psi^T \mathbf{v}_\theta, \quad (\text{C } 3b)$$

$$\mathbf{u}_z(\mathbf{x}, t) = \sum_{k=1}^{n_v} \psi^k(\mathbf{x}) v_z^k(t) = \Psi^T \mathbf{v}_z, \quad (\text{C } 3c)$$

$$\mathbf{p}(\mathbf{x}, t) = \sum_{l=1}^{n_p} \lambda^l(\mathbf{x}) \mathbf{p}^l(t) = \Lambda^T \mathbf{p}, \quad (\text{C } 3d)$$

$$h = \sum_{k=1}^{n_h} \eta_k(\mathbf{r}_b) \tilde{h}_k(t) = \boldsymbol{\eta}^T \mathbf{h}, \quad (\text{C } 3e)$$

$$\Phi_r = \psi^k, \quad \Phi_\theta = \psi^k, \quad \Phi_z = \psi^k \quad \forall \quad k = 1, \dots, n_v; \quad (\text{C } 4a)$$

$$\varphi = \lambda^l \quad \forall \quad l = 1, \dots, n_p; \quad (\text{C } 4b)$$

$$\xi = \eta_m \quad \forall \quad m = 1, \dots, n_h. \quad (\text{C } 4c)$$

In equations (C 3) and (C 4a), ψ , λ and η are the shape functions for the velocity components, pressure, and interface deformation magnitude, respectively; n_v , n_p and n_h are the number of nodes for the velocity components, pressure, and interface deformation magnitude, respectively, and $v_j \forall j = r, \theta, z$, \mathbf{p} and \tilde{h} are the corresponding unknown nodal parameters of the velocity components, pressure, and interface deformation magnitude. $\mathbf{v}_i \forall i = r, \theta, z$, \mathbf{p} and \mathbf{h} are column vectors of the unknown nodal parameters for the velocity components, pressure, and interface deformation magnitude, respectively; and Ψ , Λ and $\boldsymbol{\eta}$ are the column vectors of the shape functions for the velocity components, pressure, and interface deformation magnitude, respectively.

It is seen that the shape functions for the velocity components are the same but differ from that of the pressure. This is to avoid having an over-constrained system of discrete equations. In fact, the shape function used for pressure must be at least one order lower than that of the velocity field (Reddy & Gartling 2010).

Using equations (C 3) and (C 4a), we can derive, for example, the finite element model for the continuity equation by writing the weak form of it (2.37) over an element and substituting (C 3) and (C 4a) to get

$$\left[\int_{\Omega^e} \left\{ \Lambda \left(\frac{\partial \Psi^T}{\partial r} + \frac{\Psi^T}{r} \right) \right\} d\Omega^e \right] \mathbf{v}_r + \left[\int_{\Omega^e} \left\{ i m \Lambda \frac{\Psi^T}{r} \right\} d\Omega^e \right] \mathbf{v}_\theta + \left[\int_{\Omega^e} \left\{ \Lambda \frac{\partial \Psi^T}{\partial z} \right\} d\Omega^e \right] \mathbf{v}_z = \mathbf{0}, \quad (\text{C } 5)$$

which can be compactly written as

$$\mathbf{Q}^T \mathbf{v} = \mathbf{0}, \quad (\text{C } 6)$$

where $\mathbf{v} = \begin{bmatrix} \mathbf{v}_r \\ \mathbf{v}_\theta \\ \mathbf{v}_z \end{bmatrix}$ and $\mathbf{Q} = \begin{bmatrix} \mathbf{Q}_r \\ \mathbf{Q}_\theta \\ \mathbf{Q}_z \end{bmatrix}$. $\mathbf{Q}_i \quad \forall i = r, \theta, z$ are the coefficient matrices for the

velocity components. Similar compact relations to (C 6) can be derived for the momentum equations and the kinematic boundary condition. The combined formed of which is given in equation (2.39) and full expressions for the terms are:

continuity equation

$$\mathbf{Q}_r = \int_{\Omega^{0,e}} \left\{ \Lambda \left(\frac{\partial \Psi^T}{\partial r} + \frac{\Psi^T}{r} \right) \right\} d\Omega^{0,e}, \quad (\text{C } 7)$$

$$\mathbf{Q}_\theta = \int_{\Omega^{0,e}} \left\{ im\Lambda \frac{\Psi^T}{r} \right\} d\Omega^{0,e}, \quad (\text{C } 8)$$

$$\mathbf{Q}_z = \int_{\Omega^{0,e}} \left\{ \Lambda \frac{\partial \Psi^T}{\partial z} \right\} d\Omega^{0,e}, \quad (\text{C } 9)$$

$$\mathbf{Q}_p = \int_{\Omega^{0,e}} \left\{ \varepsilon \Lambda \Lambda^T \right\} d\Omega^{0,e}; \quad (\text{C } 10)$$

momentum equation: growth rate part

$$\mathbf{B}_{i,i} = \int_{\Omega^{0,e}} \left\{ \Psi \Psi^T \right\} d\Omega^{0,e} \quad \forall i = r, \theta, z, \quad (\text{C } 11)$$

momentum equation: convective part

$$\mathbf{C}_{i,i} = \int_{\Omega^{0,e}} \left\{ \Psi \left[(\mathbf{u}^0 \cdot \nabla) \Psi^T + \delta_{r,i} \Psi^T \frac{\partial u_r^0}{\partial r} + \delta_{z,i} \Psi^T \frac{\partial u_z^0}{\partial z} \right] \right\} d\Omega^{0,e} \quad \forall i = r, z, \quad (\text{C } 12)$$

$$\mathbf{C}_{\theta,\theta} = \int_{\Omega^{0,e}} \left\{ \Psi \left[(\mathbf{u}^0 \cdot \nabla) \Psi^T + \frac{u_r^0 \Psi^T}{r} \right] \right\} d\Omega^{0,e}, \quad (\text{C } 13)$$

$$\mathbf{C}_{r,z} = \int_{\Omega^{0,e}} \left\{ \Psi \Psi^T \frac{\partial u_r^0}{\partial z} \right\} d\Omega^{0,e}, \quad (\text{C } 14)$$

$$\mathbf{C}_{z,r} = \int_{\Omega^{0,e}} \left\{ \Psi \Psi^T \frac{\partial u_z^0}{\partial r} \right\} d\Omega^{0,e}; \quad (\text{C } 15)$$

momentum equation: viscous part

$$\begin{aligned} \mathbf{K}_{i,i} = \int_{\Omega^{0,e}} Nf^{-1} \left\{ 2 \frac{\partial \Psi}{\partial i} \frac{\partial \Psi^T}{\partial i} + (2\delta_{r,i} + m^2) \frac{\Psi \Psi^T}{r^2} + \delta_{r,i} \frac{\partial \Psi}{\partial z} \frac{\partial \Psi^T}{\partial z} + \delta_{z,i} \frac{\partial \Psi}{\partial r} \frac{\partial \Psi^T}{\partial r} \right. \\ \left. + \delta_{z,i} \frac{\partial \Psi}{\partial r} \frac{\partial \Psi^T}{\partial r} \right\} d\Omega^{0,e} \quad \forall i = r, z, \end{aligned} \quad (\text{C } 16a)$$

$$\begin{aligned} \mathbf{K}_{\theta,\theta} = \int_{\Omega^{0,e}} Nf^{-1} \left\{ (1 + 2m^2) \frac{\Psi \Psi^T}{r^2} + \frac{\partial \Psi}{\partial z} \frac{\partial \Psi^T}{\partial z} + \frac{\partial \Psi}{\partial r} \frac{\partial \Psi^T}{\partial r} \right. \\ \left. - \left(\frac{\Psi^T}{r} \frac{\partial \Psi}{\partial r} + \frac{\Psi}{r} \frac{\partial \Psi^T}{\partial r} \right) \right\} d\Omega^{0,e}, \end{aligned} \quad (\text{C } 16b)$$

$$\mathbf{K}_{r,z} = \int_{\Omega^{0,e}} Nf^{-1} \left\{ \frac{\partial \Psi}{\partial z} \frac{\partial \Psi^T}{\partial r} \right\} d\Omega^{0,e}, \quad (\text{C } 16c)$$

$$\mathbf{K}_{i,\theta} = \int_{\Omega^{0,e}} Nf^{-1} \left\{ \delta_{r,i} 3im \frac{\Psi \Psi^T}{r^2} - im \frac{\Psi}{r} \frac{\partial \Psi^T}{\partial i} \right\} d\Omega^{0,e} \quad \forall i = r, z; \quad (\text{C } 16d)$$

momentum equation: interface deformation part

$$\begin{aligned}
\mathbf{M}_{i,h} = & - \int_{\Gamma_b^{0,e}} Eo^{-1} \left\{ - \left[n_i \frac{d\Psi}{ds} - \kappa_a (t_i \Psi) \right] \frac{d\boldsymbol{\eta}^T}{ds} + n_i \left[\kappa_a^2 + \kappa_b^2 - \frac{m^2}{r^2} \right] \Psi \boldsymbol{\eta}^T \right\} d\Gamma_b^{0,e} \\
& - \int_{\Gamma_b^0} \{ n_z n_i \Psi \boldsymbol{\eta}^T \} d\Gamma_b^0 \\
& + \int_{\Gamma_b^0} \left\{ \left\{ (u_i^0 t_i) \left[\frac{du_i^0}{ds} \Psi \right] + \left[-p^0 + 2Nf^{-1} \left(t_i \frac{du_i^0}{ds} \right) \right] \left(t_i \frac{d\Psi}{ds} \right) \right\} \boldsymbol{\eta}^T \right\} d\Gamma_b^0 \\
& + \int_{\Gamma_b^0} \left\{ \left[Eo^{-1} \kappa + z - P_b^0 \right] \left[(t_i \Psi) \frac{d\boldsymbol{\eta}^T}{ds} + \kappa (n_i \Psi \boldsymbol{\eta}^T) \right] \right\} d\Gamma_b^0 \quad \forall i = r, z,
\end{aligned} \tag{C 17a}$$

$$\mathbf{M}_{\theta,h} = \int_{\Gamma_b^0} \left\{ \left[\left(-p^0 + 2Nf^{-1} \frac{u_r^0}{r} \right) - (Eo^{-1} \kappa + z - P_b^0) \right] \left(-im \frac{\Psi \boldsymbol{\eta}^T}{r} \right) \right\} d\Gamma_b^0; \tag{C 17b}$$

kinematic boundary condition

$$\mathbf{X}_i = \int_{\Gamma_b^{0,e}} n_i \{ \boldsymbol{\eta} \Psi^T \} d\Gamma_b^{0,e} \quad \forall i = r, z, \tag{C 18a}$$

$$\mathbf{X}_h = \int_{\Gamma_b^{0,e}} \left\{ (\mathbf{u}^0 \cdot \mathbf{t}) \boldsymbol{\eta} \frac{d\boldsymbol{\eta}^T}{ds} - \left(\frac{d\mathbf{u}^0}{dn} \cdot \mathbf{n} \right) \boldsymbol{\eta} \boldsymbol{\eta}^T \right\} d\Gamma_b^{0,e}, \tag{C 18b}$$

$$\mathbf{B}_h = \int_{\Gamma_b^{0,e}} \{ \boldsymbol{\eta} \boldsymbol{\eta}^T \} d\Gamma_b^{0,e}. \tag{C 18c}$$

REFERENCES

- ABUBAKAR, H. A. & MATAR, O. K. 2021 Taylor bubble motion in stagnant and flowing liquids in vertical pipes. part i: Steady-states. *Submitted to J. Fluid Mech.* .
- ANJOS, G., MANGIAVACCHI, N., BORHANI, N. & THOME, J. R. 2014 3D ALE finite-element method for two-phase flows with phase change. *Heat Transfer Engineering* **35** (5), 537–547.
- BOOMKAMP, P.A.M. & MIESEN, R.H.M. 1996 Classification of instabilities in parallel two-phase flow. *Int. J. Multiphase Flow* **22**, 67–88.
- BROWN, R.A.S. 1965 The mechanics of large gas bubbles in tubes I. Bubble velocities in stagnant liquids. *Can. J. Chem. Eng* **43**, 217–223.
- BUGG, J. D. & SAAD, G. A. 2002 The velocity field around a Taylor bubble rising in a stagnant viscous fluid: Numerical and experimental results. *Int. J. Multiphase Flow* **28**, 791–803.
- CAIRNCROSS, R.A., SCHUNK, P.R., BAER, T.A., RAO, R.R. & SACKINGER, P.A. 2000 A finite element method for free surface flows of incompressible fluids in three dimensions. Part I. Boundary fitted mesh motion. *Int. J. Numer. Meth. Fluids* **33**, 375–403.
- CAMPOS, J.B.L.M. & GUEDES DE CARVALHO, J.R.F. 1988 An experimental study of the wake of gas slugs rising in liquids. *J. Fluid Mech.* **196**, 27–37.
- CARVALHO, M.S. & SCRIVEN, L.E. 1999 Three-dimensional stability analysis of free surface flows: application to forward deformable roll coating. *J. Comput. Phys.* **151**, 534–562.
- CHIREUX, V., FABRE, D., RISSO, F. & TORDJEMAN, P. 2015 Oscillations of a liquid bridge resulting from the coalescence of two droplets. *Physics of Fluids* **27**, 062103.
- CHRISTODOULOU, C.N. & SCRIVEN, L.E. 1988 Finding leading modes of a viscous free surface flow: An asymmetric generalized eigenproblem. *J. Sci. Comput.* **3** (4), 355–406.
- COLLINS, R., DE MORAES, F., DAVIDSON, J. & HARRISON, D. 1978 The motion of a large gas bubble rising through liquid flowing in a tube. *J. Fluid Mech* **89**, 497–514.
- CUVELIER, C. & SCHULKES, R.M.S.M. 1990 Some numerical methods for the computation of

- capillary free boundaries governed by the Navier-Stokes equations. *SIAM Rev.* **32** (3), 355–423.
- DUMITRESCU, D.T. 1943 Strömung an einer Luftblase im senkrechten Rohr. *Z. Angew. Math. Mech* **23** (3), 139–149.
- FABRE, J. 2016 A long bubble rising in still liquid in a vertical channel: a plane inviscid solution. *J. Fluid Mech.* **794**, R4.
- FABRE, J. & FIGUEROA-ESPINOZA, B. 2014 Taylor bubble rising in a vertical pipe against laminar or turbulent downward flow: symmetric to asymmetric shape transition. *J. Fluid Mech.* **755**, 485–502.
- FERSHTMAN, A., BABIN, V., BARNEA, D. & SHEMER, L. 2017 On shapes and motion of an elongated bubble in downward liquid pipe flow. *Physics of Fluids* **29**, 112103.
- FIGUEROA-ESPINOZA, B. & FABRE, J. 2011 Taylor bubble moving in a flowing liquid in vertical channel: transition from symmetric to asymmetric shape. *J. Fluid Mech.* **679**, 432–454.
- FUNADA, T., JOSEPH, D., MAEHARA, T. & YAMASHITA, S. 2005 Ellipsoidal model of the rise of a Taylor bubble in a round tube. *Int. J. Multiph. Flow* **31**, 473–491.
- GRIFFITH, P. & WALLIS, G. B. 1961 Two phase slug flow. *ASME: J. Heat Transfer* **83**, 07–320.
- HA NGOC, H. & FABRE, J. 2006 A boundary element method for calculating the shape and velocity of two-dimensional long bubble in stagnant and flowing liquid. *Engng Anal. Bound. Elem.* **30**, 539–552.
- HEINRICH, J.C. & PEPPER, D.W. 1999 *Intermediate finite element method : fluid flow and heat transfer applications*. Taylor & Francis Group.
- HOOPER, A.P. & BOYD, W.G.C. 1983 Shear-flow instability at the interface between two viscous fluids. *J. Fluid Mech.* **128**, 507–528.
- HU, H.H & JOSEPH, D.D. 1989 Lubricated pipelining: stability of core-annular flow. Part 2. *J. Fluid Mech.* **205**, 359–396.
- KANG, C.W., QUAN, S.P. & LOU, J. 2010 Numerical study of a Taylor bubble rising in stagnant liquids. *Phys. Rev. E* **81**, 1539–3755.
- KRUYT, N.P., CUVELIER, C., SEGAL, A. & VAN DER ZANDEN, J. 1988 A total linearization method for solving viscous free boundary flow problems by the finite-element method. *Int. J. Numer. Methods Fluids* **8**, 351–363.
- LEHOUCQ, R.B., SORENSEN, D.C. & YANG, C. 1997 ARPACK user's guide: solution of large scale eigenvalue problems with implicitly restarted Arnoldi methods. *SIAM* .
- LIZARRAGA-GARCIA, E., BUONGIORNO, J., AL-SAFRAN, E. & LAKEHAL, D. 2017 A broadly applicable unified closure relation for Taylor bubble rise velocity in pipes with stagnant liquid. *Int. J. Multiph. Flow* **89**, 345–358.
- LLEWELLIN, E.W., DEL BELLO, E., TADDEUCCI, J., SCARLATO, P. & LANE, S.J. 2012 The thickness of the falling film of liquid around a Taylor bubble. *Proc. R. Soc. A* **468**, 1041–1064.
- LU, X & PROSPERETTI, A. 2006 Axial stability of Taylor bubbles. *J. Fluid Mech.* **568**, 173–192.
- LU, X & PROSPERETTI, A. 2009 A numerical study of Taylor bubbles. *Ind. Eng. Chem. Res.* **48**, 242–252.
- MAO, Z.S. & DUKLER, A.E. 1990 The motion of Taylor bubbles in vertical tubes I. A numerical simulation for the shape and rise velocity of Taylor bubbles in stagnant and flowing liquids. *J. Comput. Phys.* **91**, 2055–2064.
- MAO, Z.S. & DUKLER, A.E. 1991 The motion of Taylor bubbles in vertical tubes II. Experimental data and simulations for laminar and turbulent flow. *Chem. Eng. Sci.* **46**, 132–160.
- MARTIN, C.S. 1976 Vertically downward two-phase slug flow. *Trans. ASME J. Fluids Engng* **98**, 715–722.
- MILLER, C.A. & SCRIVEN, L.E. 1968 The oscillations of a fluid droplet immersed in another fluid. *J. Fluid Mech.* **32**, 417–435.
- MOISSIS, R. & GRIFFITH, P. 1962 Entrance effect in a two-phase slug flow. *J. Heat Transf.* **84**, 29–38.
- NATARAJAN, R. 1992 An Arnoldi-based iterative scheme for nonsymmetric matrix pencils arising in finite element stability problems. *J. Comput. Phys.* **100**, 128–142.
- NICKLIN, D., WILKES, J. & DAVIDSON, J. 1962 Two-phase flow in vertical tubes. *Trans. Inst. Chem. Engrs* **40**, 61–68.

- NIGMATULIN, T.R. 2001 Surface of a Taylor bubble in vertical cylindrical flows. *Dokl. Phys.* **46**, 803–805.
- NOGUEIRA, S., RIETHMULLER, M.L., CAMPOS, J.B.L.M. & PINTO, A.M.F.R. 2006 Flow patterns in the wake of a Taylor bubble rising through vertical columns of stagnant and flowing Newtonian liquids: an experimental study. *Chem. Eng. Sci.* **61**, 7199–7212.
- Ó NÁRAIGH, L., SPELT, P.D.M., MATAR, O. K. & ZAKI, T.A. 2011 Interfacial instability in turbulent flow over a liquid film in a channel. *Int. J. Multiphase Flow* **37**, 812–830.
- POLONSKY, S., SHEMER, L. & BARNEA, D. 1999 The relation between the Taylor bubble motion and the velocity field ahead of it. *Int. J. Multiphase Flow* **25**, 957–975.
- POZRIKIDIS, C. 2011 *Introduction to theoretical and computational fluid dynamics*. Taylor & Francis Group.
- PRINGLE, C.C.T., AMBROSE, S., AZZOPARDI, B.J. & RUST, A.C. 2015 The existence and behaviour of large diameter Taylor bubbles. *Int. J. Multiphase Flow* **72**, 318–323.
- PROSPERETTI, A. 1980 Normal-mode analysis for the oscillations of a viscous liquid drop in an immiscible liquid. *Journal de Mécanique* **19** (1), 149–181.
- RAMANAN, N. & ENGELMAN, M.S. 1996 An algorithm for simulation of steady free surface flows. *Int. J. Numer. Methods Fluids* **22**, 103–120.
- RANA, B.K., DAS, A.K. & DAS, P.K. 2015 Mechanism of bursting Taylor bubbles at free surfaces. *Langmuir* **31**, 9870–9881.
- REDDY, J.N. & GARTLING, D.K. 2010 *The finite element method in heat transfer and fluid dynamics*. Taylor & Francis Group.
- SAHU, K.C., DING, H., VALLURI, P. & MATAR, O.K. 2009 Linear stability analysis and numerical simulation of miscible two-layer channel flow. *Physics of Fluids* **21**, 042104.
- SAHU, K.C., VALLURI, P., SPELT, P.D.M. & MATAR, O.K. 2007 Linear instability of pressure-driven channel flow of a newtonian and Herschel-Bulkley fluid. *Physics of Fluids* **19**, 122101.
- SELVAM, B., MERK, S., GOVINDARAJAN, R. & MEIBURG, E. 2007 Stability of miscible core-annular flows with viscosity stratification. *J. Fluid Mech.* **592**, 23–49.
- TAHA, T. & CUI, Z.F. 2006 CFD modeling of slug flow in vertical tubes. *Chem. Eng. Sci.* **61**, 676–687.
- WEATHERBURN, C.E. 1927 *Differential geometry of three dimensions*. UK: Cambridge University press, part 127, pp 251.
- WHITE, E.T. & BEARDMORE, R.H. 1962 The velocity of rise of single cylindrical air bubbles through liquids contained in vertical tubes. *Chem. Eng. Sci.* **17**, 351–361.